Bull Volcanol (2009) 71:49–77
DOI 10.1007/s00445-008-0209-y

RESEARCH ARTICLE

Eruptive conditions and depositional processes of Narbona Pass Maar volcano, Navajo volcanic field, Navajo Nation, New Mexico (USA)

Brittany D. Brand · Amanda B. Clarke · Steven Semken

Received: 20 April 2007 / Accepted: 31 January 2008 / Published online: 24 May 2008

Abstract Phreatomagmatic deposits at Narbona Pass, a mid-Tertiary maar in the Navajo volcanic field (NVF), New Mexico (USA), were characterized in order to reconstruct the evolution and dynamic conditions of the eruption. Our findings shed light on the temporal evolution of the eruption, dominant depositional mechanisms, influence of liquid water on deposit characteristics, geometry and evolution of the vent, efficiency of fragmentation, and the relative importance of magmatic and external volatiles. The basal deposits form a thick (5–20 m), massive lapilli tuff to tuff-breccia deposit. This is overlain by alternating bedded sequences of symmetrical to antidune cross-stratified tuff and lapilli tuff; and diffusely-stratified, clast-supported, reversely-graded lapilli tuffs that pinch and swell laterally. This sequence is interpreted to reflect an initial vent-clearing phase that produced concentrated pyroclastic density currents, followed by a pulsating eruption that produced multiple density currents with varying particle concentrations and flow conditions to yield the well-stratified deposits. Only minor localized soft-sediment deformation was observed, no accretionary lapilli were found, and grain accretion occurs on the lee side of dunes. This suggests that little to no liquid water existed in the density currents during deposition. Juvenile material is dominantly present as blocky fine ash and finely vesiculated fine to coarse lapilli pumice. This indicates that phreatomagmatic fragmentation was predominant, but also that the magma was volatile-rich and vesiculating at the time of eruption. This is the first study to document a significant magmatic volatile component in an NVF maar-diatreme eruption. The top of the phreatomagmatic sequence abruptly contacts the overlying minette lava flows, indicating no gradual drying-out period between the explosive and effusive phases. The lithology of the accidental clasts is consistent throughout the vertical pyroclastic stratigraphy, suggesting that the diatreme eruption did not penetrate below the base of the uppermost country rock unit, a sandstone aquifer ~360 m thick. By comparison, other NVF diatremes several tens of kilometers away were excavated to depths of ~1,000 m beneath the paleosurface (e.g., Delaney PT. Ship Rock, New Mexico: the vent of a violent volcanic eruption. In: Beus SS (ed) Geological society of America Centennial Field Guide, Rocky Mountain Section 2:411–415 (1987)). This can be accounted for by structurally controlled variations in aquifer thickness beneath different regions of the volcanic field. Variations in accidental clast composition and bedding style around the edifice are indicative of a laterally migrating or widening vent that encountered lateral variations in subsurface geology. We offer reasonable evidence that this subsurface lithology controlled the availability of external water to the magma, which in turn controlled characteristics of deposits and their distribution around the vent.

Keywords Phreatomagmatic · Maar · Narbona Pass · Minette · Pyroclastic · Base surge · Navajo volcanic field

Editorial responsibility: J. White

Electronic supplementary material The online version of this article (doi:10.1007/s00445-008-0209-y) contains supplementary material, which is available to authorized users.

B. D. Brand (✉) · A. B. Clarke · S. Semken
School of Earth and Space Exploration, Arizona State University, Tempe, AZ 85287-1404, USA
e-mail: bbrand@asu.edu

Introduction

Phreatomagmatic eruptions occur when rising magma mixes with shallow surface water or groundwater (Sheridan and Wohletz 1983). Controlled experiments demonstrate

that the degree of fragmentation associated with the magma–water interaction, as evidenced by particle size, is a function of melt composition, magma flux, water–melt mass ratio, confining pressure, magma viscosity, mixing efficiency, and the degree of turbulent mixing of magma with water, steam, or water sprays (Sheridan and Wohletz 1983; Wohletz and McQueen 1984; Büttner and Zimanowski 1998; Zimanowski et al. 1991; Mastin 2007). However, the challenge of identifying depositional characteristics and relationships indicative of specific vent conditions remains.

There is a significant body of literature suggesting that phreatomagmatic pyroclastic deposits can lend insight into eruptive energy, the amount of liquid water in the eruption column and flows, and the relative influence of external water at the vent (e.g., Fisher and Waters 1970; Crowe and Fisher 1973; Lorenz 1974; Sheridan and Wohletz 1983; Fisher and Schmincke 1984; Houghton and Hackett 1984; Kokelaar 1983, 1986; Sohn and Chough 1989; Dellino et al. 1990; Houghton et al. 1999; White 1996, 2001; Nemeth et al. 2001; Cole et al. 2001; Mastin et al. 2004; Brand and White 2007). It has been variously suggested that many characteristics of phreatomagmatic pyroclastic deposits, such as the presence or absence of features associated with liquid water (i.e., accretionary lapilli and bomb sags), bedding characteristics, and edifice morphology; can be attributed to the original amount of external water-to-melt mass ratio (Heiken 1971; Wohletz and McQueen 1984; Sheridan and Wohletz 1983). This ratio may change many times throughout an eruption as a result of increasing or decreasing magma mass flux (Kokelaar 1983, 1986), an increase or decrease in the source and abundance of external water (Brand and White 2007), fluctuations in mixing efficiency and turbulence (Büttner and Zimanowski 1998; Mastin et al. 2004), variable influence of magmatic volatiles in fragmentation (Houghton et al. 1999; Houghton and Hackett 1984; Houghton and Schmincke 1986; Houghton and Wilson 1989), and the relative effectiveness of vent sealing against external water (Cole et al. 2001; Brand and White 2007).

This study is intended to build on the existing framework for hydromagmatic pyroclastic deposits and to continue to identify relationships between deposit characteristics and eruptive dynamics of mafic phreatomagmatic eruptions. To this end, we have examined the well-preserved Oligocene tephras of the Narbona Pass maar volcano (NPM), a center in the Navajo volcanic field (NVF) located in northwestern New Mexico, to better understand its eruptive history and the phreatomagmatic processes that operated during the eruption. We look specifically at the temporal evolution of the eruption, dominant depositional mechanisms, the influence of liquid water on deposit characteristics, vent geometry and evolution, and the relative importance of magmatic and external volatiles in fragmentation.

The occurrence of highly potassic, phlogopite-bearing minette provides an additional reason to study the eruptive history of NPM. Minette magmas have been interpreted to originate from a mantle source, based on their mafic and ultramafic xenoliths, high Mg-numbers, and Ni and Cr contents (Esperanca and Holloway 1987; Ehrenberg 1978; Best and Christiansen 2001). The source region for NVF minettes is thought to have undergone several episodes of metasomatism and melt depletion (Roden 1981; Carlson and Nowell 2001). The sensitivity of phase assemblages in minettes with both olivine and phlogopite phenocrysts, such as those from NPM (Ehrenberg 1978), suggest eruption at high, near liquidus temperatures (Esperanca and Holloway 1987), which implies fast ascent rates from the mantle. Furthermore, the original content of CO_2 and H_2O of these magmas is in some cases argued to drive fragmentation (Gonzales et al. 2006), and in other cases interpreted to aid in fragmentation efficiency during phreatomagmatic eruptions (Shaanan et al. 2007).

Geologic setting

NPM is one of approximately 80 volcanic and hypabyssal features in the Oligocene–Miocene NVF (Semken 2003) in the central Colorado Plateau, and is located atop the East Defiance monocline in the Chuska Mountains, Navajo Nation, New Mexico, USA (Fig. 1a). NVF rocks are mostly potassic lamprophyres, dominated by hypabyssal and extrusive mafic minettes and ultramafic microbreccias (Smith and Levy 1976). Other NVF centers in the vicinity of NPM, such as the iconic Ship Rock monolith 67 km to the north, are exhumed minette tuff-breccia diatremes. It is reasonable to presume that NPM was fed by a similar diatreme (Ehrenberg 1978; Semken 2003) consistent with the Lorenz (1986) model. The NPM volcanic center consists of a thick sequence of bedded tuffs capped by three minette lava flows (Fig. 1b) and minor minette plugs (Appledorn and Wright 1957; Ehrenberg 1978). The oldest lava flow has an $^{40}Ar/^{39}Ar$ age of 25.05±0.16 Ma (Cather et al. 2003).

NPM is directly underlain by the Chuska Sandstone, an Eocene–Oligocene formation that caps most of the mountain range. The Chuska Sandstone is divided into two members: the upper, eolian Narbona Pass Member, and the lower, fluviatile Deza Member (Fig. 2; Wright 1956; Lucas and Cather 2003). The Narbona Pass Member, which is ~360 m thick at NPM (Lucas and Cather 2003), is a pinkish-grey to yellowish-grey trough cross-bedded arkosic sandstone that ranges from strongly indurated to friable (Wright 1956; Trevena and Nash 1979; Lucas and Cather 2003).

The basal Deza Member is 81 m thick or less and occurs only in scattered paleovalleys in the pre-Chuska surface

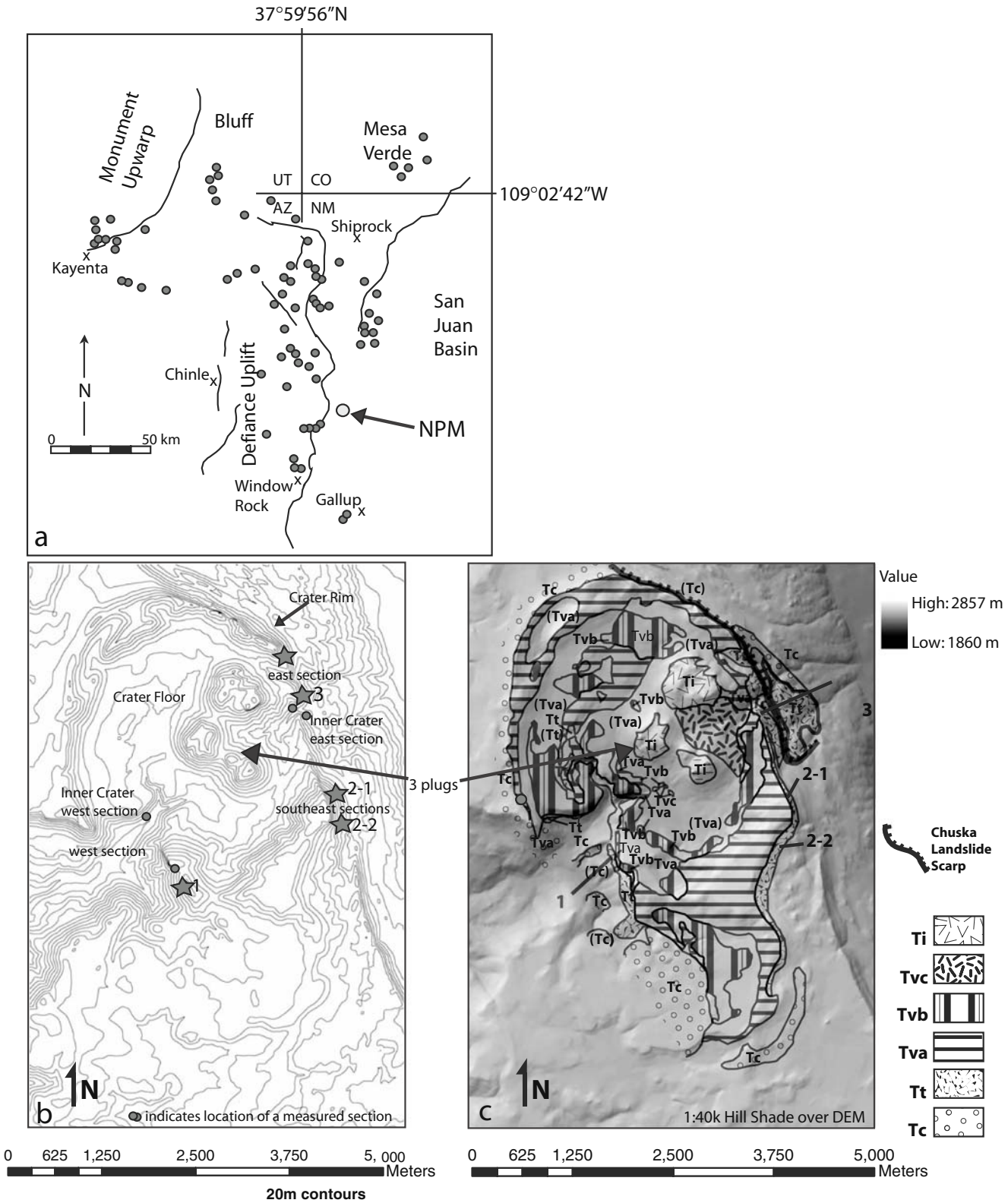

Fig. 1 **a** Map of the main part of the Navajo volcanic field (after Semken 2003). Extrusive and intrusive features are shown as *black circles*; location of NPM (36°05.5′ N, 108°51.5′ W) is shown as a *gray circle*; *black lines* indicate regional Laramide monoclines; *x*'s indicate towns. **b** Topographic map of NPM (U.S. Geological Survey. *Narbona Pass, or Washington Pass, New Mexico.* 1:24,000. 7.5 Minute Series. Washington D.C.: USGS 1992). *Stars* identify locations of sections measured in this study. **c** Geologic map overlain on DEM of NPM (from Ehrenberg 1978 and Lucas et al. 2003). *Tc* Chuska Sandstone, *Tt* NPM pyroclastic deposits, *Tva*, *Tvb*, and *Tvc* lava flows described in the text, and *Ti* plugs described in text

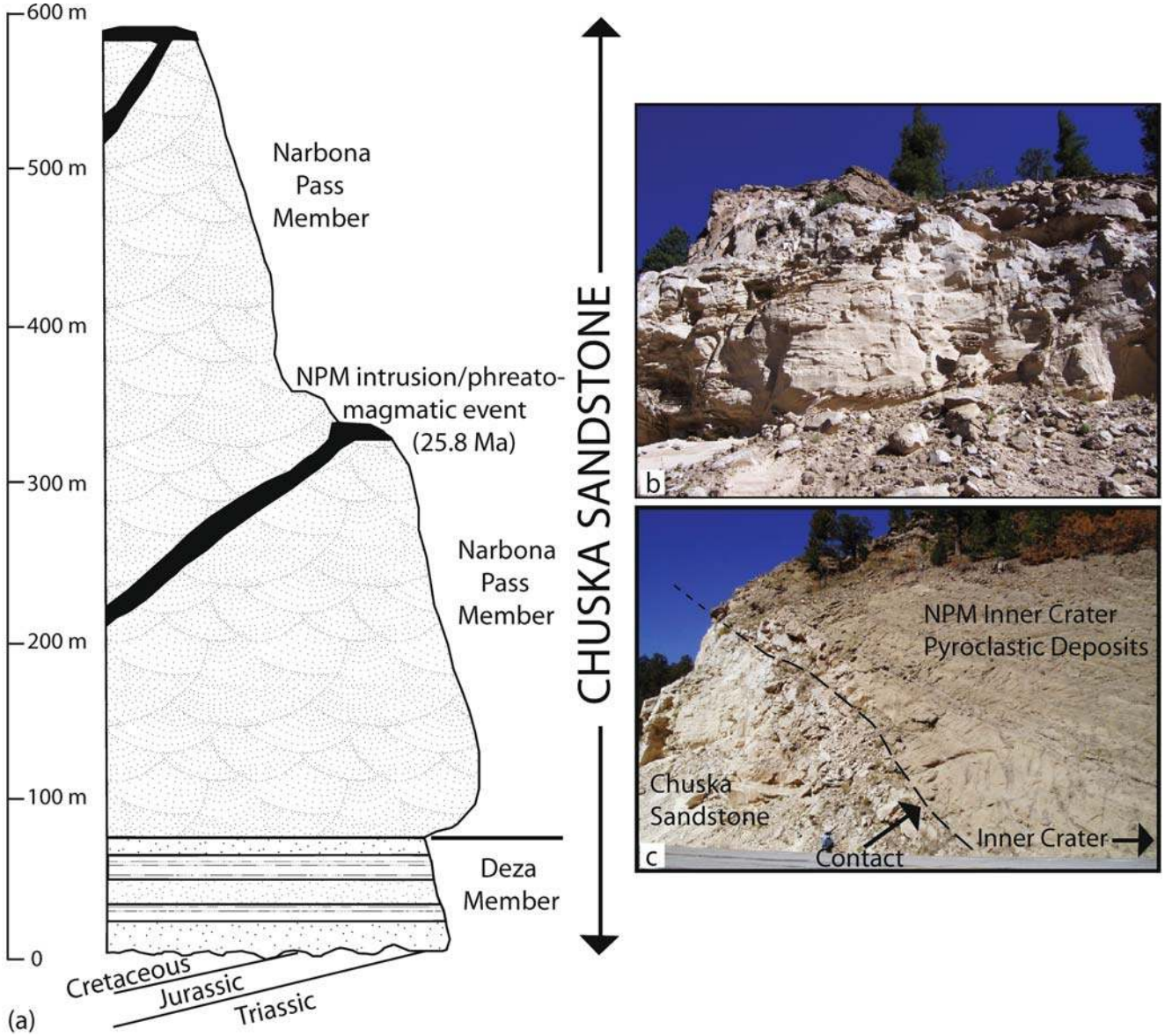

Fig. 2 **a** Stratigraphy in the vicinity of NPM [after Lucas and Cather (2003) and Trevena and Nash (1979)]. Mesozoic units are not shown to scale. **b** Large scale foreset cross-beds within the Narbona Pass Member of the Chuska Sandstone (outcrop is approximately 15 m high). **c** NPM pyroclastic deposits cutting the Chuska Sandstone (roadcut is in the west rim of the crater; vent focus ~0.5–1 km to the right; *person at bottom center* indicates scale)

(Lucas and Cather 2003). It is not exposed at NPM, but crops out in the Crystal Creek drainage several kilometers to the west. It consists mostly of arkosic sandstone beds with minor interbedded siltstone and claystone (Wright 1956; Lucas and Cather 2003). Where the Deza Member is present, the contact with the overlying Narbona Pass Member is conformable (Fig. 2; Wright 1956).

The Chuska Sandstone was deposited atop a regional erosion surface (the Tsaile surface of Schmidt 1991) that bevels Cretaceous to Triassic rocks in the eastward-dipping limb of the East Defiance monocline. Mesozoic stratigraphy directly beneath NPM is not well exposed (Fig. 2), but on the basis of outcrops to the west, it is presumed to be composed of Upper Cretaceous Mancos Shale and Dakota Sandstone; Upper Jurassic Morrison Formation; Middle Jurassic Zuni Sandstone; and Upper Triassic Wingate Sandstone and Chinle Group.

Data

Centimeter-scale measurements of four inner crater and five outer crater proximal sections (Fig. 1b) of the NPM pyroclastic deposits yielded 35 lithofacies. The lithofacies

were grouped into facies associations (FA) according to common bedding styles, fragment morphology, and the percentage and type of accidental components. FAs differ from units in that they may repeat several times throughout the section.

Inner crater tuff ring deposits

The inner crater deposits are exposed on both the east and west sides of the eroded maar, where they dip 25–31° towards the center of the crater. The contact between Chuska Sandstone and NPM tuff is exposed on the west side of the edifice where the pyroclastic deposits cut through the older sandstone (Fig. 1c). This indicates that the crater floor is below the original surrounding surface, and thus that NPM is a true maar (Cas and Wright 1987). Fourteen lithofacies were identified within the inner crater deposits, and various combinations of these were grouped into six FAs (Tables 1 and 2).

The inner crater deposits are primarily massive lapilli tuffs and tuff breccia with minor components of cross-bedded and plane-parallel bedded deposits. Inner crater deposits tend to be thick and poorly sorted, show both normal grading (in beds 0.5–4 m thick) and reverse grading (in beds <1 m thick), and commonly truncate underlying strata. While these deposits contain some primary features, most are interpreted to have resulted from syn-eruptive inward avalanching of erupted tephras down steep slopes of the inner crater (Table 2). This is indicated by the massive, poorly sorted nature of the deposits, rounded grains, occasional breccias, and thickening of massive beds towards the inner vent. The cross- and planar-bedded deposits present in localized areas are evidence for simultaneous lateral flow of density currents and fallout from the vent. Detailed descriptions and interpretations of these FAs and their lithofacies can be found in the supplemental material (Supplemental tables 1 and 2), but as most of the deposits are interpreted to record recycling and avalanching of material down the inner slopes, rather than primary depositional features recording changes in the eruption, they will not be discussed further in this paper.

Outer crater tuff ring deposits

The primary foci of this study are the outer crater deposits and their distribution around the vent, as they dominantly exhibit primary depositional characteristics and thus record the original sequence of eruptive events. Twenty-two outer-crater phreatomagmatic lithofacies and four magmatic lithofacies were identified (Table 1). These lithofacies are grouped into four FAs (Table 2).

Facies associations: descriptions and interpretations

PH1: massive pyroclastic deposits

PH1 contains matrix-supported lapilli tuffs and tuff-breccias (Fig. 3). Most exposures of PH1 are between 15–20 m thick, massive, poorly sorted; and generally ungraded except for a slight fining upward of the coarse clasts representing crude coarse-tail grading (Fig. 3c). In these occurrences, the base of the unit consists of coarse lapilli to fine blocks in a matrix of fine to coarse ash (between 10–25% fine blocks, less commonly medium blocks). The clast sizes decrease upward throughout the FA to dominantly medium lapilli with <5% fine blocks. The amount of matrix is highly variable and composes between 40–80% of the deposits, while the clasts compose the remaining 20–60%. Infrequent, clast-supported, diffusely-stratified interbeds 0.05 – 0.5 m thick are also present (Fig. 3a). They contain 80% clasts ranging from coarse ash to fine blocks (average grain size: fine to medium lapilli) with ~20% fine to medium ash matrix.

In other, less-common exposures, PH1 beds are 0.5–1 m thick, massive, matrix-supported, and poorly sorted with an average grain size of fine to medium lapilli within a matrix of 50–60% fine ash. These thinner beds are bounded by fines-dominated, crudely stratified to well-stratified beds that pinch and swell laterally (Fig. 3b,c). Fine to medium lapilli stringers occur sparsely within these deposits. The thinner deposits are often directly overlain by the thicker deposits described above.

Clasts within PH1 are dominantly angular to subangular, with less common subrounded accidental lithics, and juvenile scoria and pumice. The compositions and percentages of juvenile and accidental lithics are described in detail in the clast analysis section below. However, it is relevant here to note that between 25–30% of the grains found in this FA were either juvenile scoria or finely vesiculated juvenile pumice (average grain size: coarse ash to fine lapilli), and up to 75% of clasts were entrained accidentals. Furthermore, no accretionary lapilli or soft-sediment deformation structures were found in PH1.

PH1 interpretation

The poorly sorted, fines-rich composition and lack of grading in PH1 indicate that it was deposited rapidly from concentrated suspensions with little tractional transport or fluidization, such that elutriation of fines and the development of grading were inhibited. The thick, massive, generally ungraded beds are suggestive of high-concentration flows (Hein 1982; Lowe 1982), and imply deposition by one or more concentrated pyroclastic density currents (Sparks 1976;

Table 1 Outer crater lithofacies classified on the basis of grain size/abundance, sedimentary features, and dominance of juvenile fragments [table modeled after Nemeth et al. (2001) and Nemeth and White (2003)]

Pyroclastic lithofacies	>10% blocks	>75% Lapilli	25–75% Lapilli	>75% Ash	Spatter	Effusive
	Tuff breccia (TB)	Lapilli stone (LS)	Lapilli tuff (LT)	Tuff (T)		
Inner crater						
Pyroclastic—matrix supported						
Clasts dominated by accidental/xenolith lithics						
Massive	MTB1, MTB2, MTB3-J		MLT1, MLT2, MLT3			
Planar stratification						
Crude planar to wavy-planar cross stratification			MPLT4-J			
Crude planar stratification						
Planar stratification—normal grading			PXT1	PT1		
Planar stratification—reverse grading			PLT1-R			
Cross-strata—combination of climbing dunes, symmetrical, and anti-dunes			XLT1	XT1, XT2		
Clasts dominated by scoriaceous/juvenile material						
Juvenile and spatter deposits	MAG1					
Outer crater						
Pyroclastic—clast supported						
Clasts dominated by accidental/xenolith lithics						
Massive	MTB5	MLS2	MLT6			
Massive, reverse grading	MLS-TB1-R	MLS1-R	MLT7-R			
Crude planar to wavy-planar cross stratification			PXLT1			
Crude planar to wavy-planar cross stratification—reverse grading		PXLS1-R				
Planar stratification—reverse grading		PLS1-R	PLT4-R			
Cross-strata—combination of climbing dunes, symmetrical, and anti-dunes			XLT2, XLT3			
Cross-strata, reverse grading		XLS1-R				
Clasts dominated by scoriaceous/juvenile material						
Massive	MAG-1					
Pyroclastic—matrix supported						
Clasts dominated by accidental/xenolith lithics						
Massive	MTB4, MLT-TB1		MLT5			
Planar stratification			PLT3			
Crude planar to wavy-planar cross stratification			PXLT2, PXLT3			
Crude planar stratification			PLT2	T3		
Non-pyroclastic						
Lava flows						Tva, Tvb, Tvc
Plugs						Ti

Detailed descriptions of individual lithofacies are available as online supplemental material (Supplemental table 3).
M Massive, *P* planar-stratification, *X* cross-stratification, *R* reverse grading, *MAG* magmatic. For example, MTB1 is a massive tuff breccia, and PXLT1 is a planar and cross-stratified lapilli tuff.

Sparks et al. 1978; Bursik and Woods 1996; Freundt and Bursik 2001; Branney and Kokelaar 2002). The clast-supported interbeds tend to vary in thickness and pinch out laterally, which suggests lateral transport (e.g., Cas and Wright 1987). They may reflect concentrated basal zones where varying degrees of shear stresses can produce diffuse stratification parallel to bedding, and if shear stresses are high enough, cause inverse grading (Lowe 1982). However, the clasts are angular and fairly well sorted, which may also indicate a contribution of fallout from an eruption column through a density current (e.g., Valentine and Giannetti 1995). Distinct coarse-tail grading was not recognized within these deposits, and would not be expected to have developed so proximal to the source.

The thinner-bedded deposits bounded by fine-grained, diffusely-stratified to well-stratified beds suggest emplace-

Table 2 Correlated units, facies associations, lithofacies, and deposit interpretations

Crater units	Lithofacies	Facies associations description and interpretation
Inner		
Phreatomagmatic (PH)	MLT1, MLT2, MLT3, MTB1, MTB2 with common interbeds of XT1 and XT2	PH-inner 1 Massive lapilli tuff and tuff breccia varying from normal-, reverse-, and no-grading, with occasional diffuse planar- and cross-stratification. Dominated by accidental lithics. Combination of tephra fallout accumulating within the crater and avalanching of erupted tephras on steep slopes of inner crater with some influence from dilute density currents and co-surge fallout
	MTB3-J, MTB5, MAG1	PH-inner 2 Same as PH-inner 1 but dominated by juvenile lithics. Intermittent co-strombolian-phreatomagmatic activity accumulating a high percentage of juvenile tephra and scoria on inner flanks of tuff ring, possibly remobilized by avalanching into inner crater
	PT1	PH-inner 3 Matrix supported, even thickness, laterally continuous, planar stratified beds, 1–4 cm thick. Deposits consist of alternating beds of coarse ash, fine lapilli, and medium lapilli. Tephra fallout derived from a pulsating phreatomagmatic eruption
	XT1, XT2	PH-inner 4 Large, symmetrical, hummocky, and wavy cross-strata with wavelengths between 3–5 m and amplitudes between 0.5–1 m. Direction of flow upwards and out of the vent. Deposition of turbulent, dilute pyroclastic density currents and co-surge fallout derived from pulsating phreatomagmatic explosions
	PXT1, PT1, and interbeds of PLT1-R	PH-inner 5 Alternates from 3–25 cm thick, fine-grained, planar and cross-stratified ash beds with almost 100% matrix (few floating coarse ash grains, facies PXAT1), and 3 cm to 0.5 m thick, grain supported, coarse ash bed with typically no grading but occasional reverse grading. Combinations of pyroclastic density currents, and co-flow/surge fallout-derived from pulsating phreatomagmatic explosions
	PLT1-R, XLT1, MLS1 and interbeds of PXT1, PT1	PH-inner 6 Dominated by thick, coarse-grained, massive deposits between 0.5 to 2.5 m thick. Alternates between clast- and matrix-supported with no grading or internal stratification, but occasional contains diffuse stratification. Dominated by concentrated pyroclastic density currents with minor influence from dilute pyroclastic currents and fallout-derived from pulsating phreatomagmatic explosions
Outer		
Phreatomagmatic (PH)	MTB5, MLS2, MLT6, MLS-TB1-R, MLST1-R, MLT7-R, MTB4, MLT-TB1, MLT5 with common interbeds of XLT2, XLT3, PXLS1-R, PLT4-R	PH1 Massive, poorly-sorted, matrix-to-clast supported lapilli tuffs and tuff-breccias. Concentrated pyroclastic density current
	T3, PXLT1, PXLS1-R, XLT2, XLT3, XLS1-R, PXLT2, PXLT3	PH2 Cross-stratified tuffs and lapilli tuffs. Turbulent, dilute pyroclastic density current
	T3, PXLT1, PXLS1-R, XLT2, XLT3, XLS1-R, PXLT2, PXLT3, PLS1-R, PLT4-R, PLT3, PLT2, MLT5, MLS1-R, MLT7-R	PH3 Laterally continuous deposits of massive and planar beds with common interbeds of fine-grained (fine-coarse ash) cross strata. Combination of alternating concentrated and dilute pyroclastic density currents
Magmatic (M)	Tva, Tvb, Tvc	M1 Minette lava flows
	Ti	M2 Two exposed minette plugs and one dike swarm

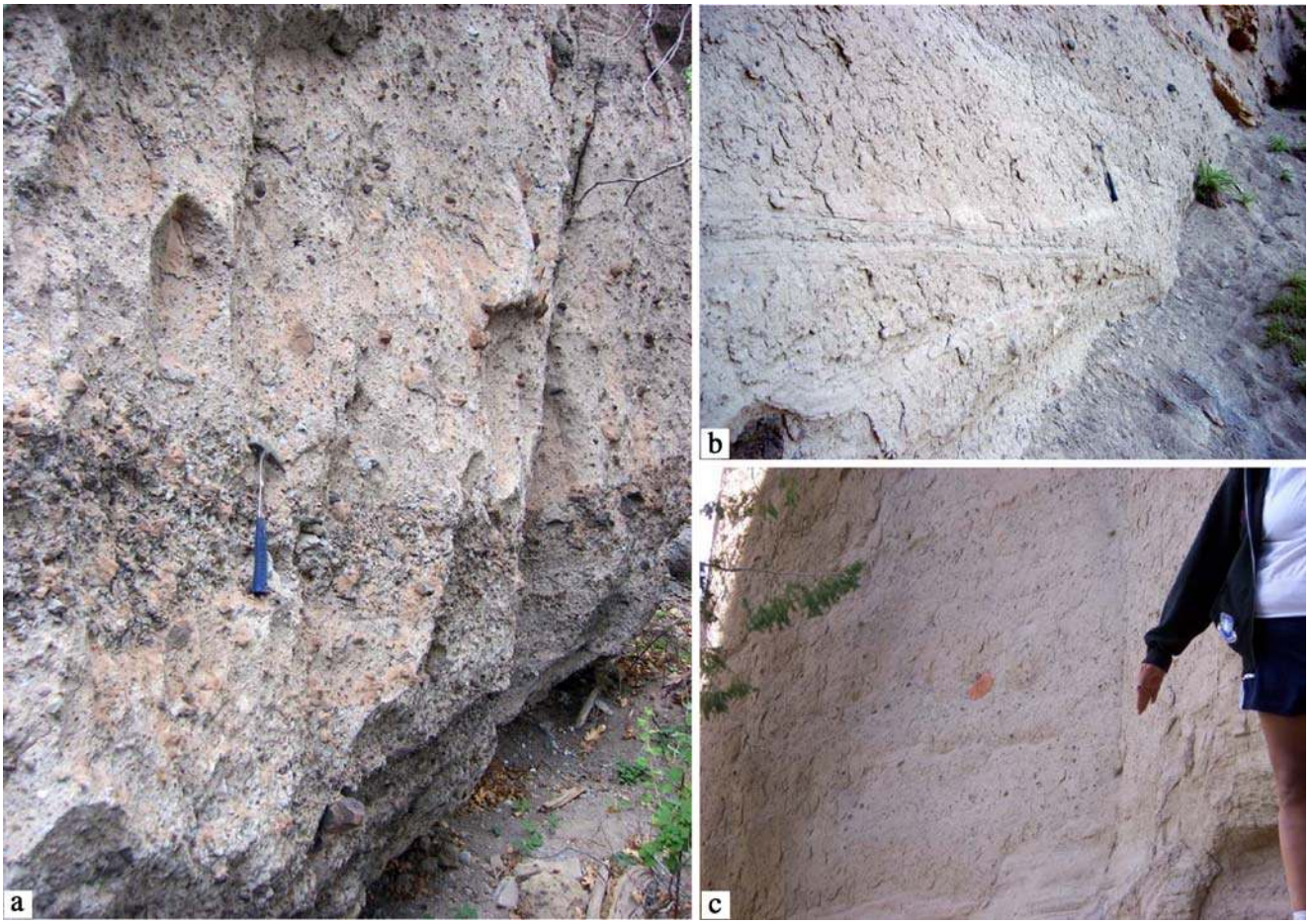

Fig. 3 **a** PH1 exposed in the east–northeast measured section (location 3 in Fig. 1b), showing a coarse, clast-supported interbed within the massive, poorly sorted deposits. **b** PH1 as exposed in the lower part of the west measured section, showing 0.5–1 m thick massive beds separated by 0.25 m finer grained, stratified beds that pinch and swell laterally. **c** PH1 exposed in the west measured section (location 1 in Fig. 1b) (*Hammer* indicates scale in **a** and **b**.)

ment of multiple density currents with little to no scouring of underlying deposits, as thinner flows bounded by fine-grained material would be easily eroded. These thin, stratified beds imply some degree of flow unsteadiness or periodicity during transport, which may be caused by local topography, obstacles, distance from the vent or eruption column, or unsteadiness at the eruption source (e.g., Fisher 1966; Sparks 1976; Sparks et al. 1978; Valentine 1987; Fisher and Schmincke 1994; Branney and Kokelaar 2002).

Because PH1 deposits lack accretionary lapilli, vesiculated fine ash tuff, and soft-sediment deformation such as ballistic clast sag structures, we interpret PH1 to have originated from pyroclastic currents with little to no liquid water present in the flow. The relatively high abundance (25–30%) of vesiculated juvenile material (20–60% vesicles), along with abundant entrained accidental lithics and angular ash morphology, suggest that vesiculation occurred before or simultaneously with phreatomagmatic fragmentation (e.g., Cole et al. 2001; Houghton and Hackett 1984).

PH2: cross-bedded pyroclastic deposits

PH2 is dominated by low-angle, cross-stratified lapilli tuffs (Fig. 4). Cross strata are abundant, with wavelengths of <1 to 6 m, and amplitudes from 0.1 to 1 m. The dune forms are elongated on both the lee and stoss sides and show both lee-side and stoss-side accretion, although lee-side accretion is dominant. These beds pinch and swell laterally along with coarse-grained, massive interbeds (described below), and commonly display a minor degree of soft-sediment deformation in regions where they are overlain by fine blocks or coarse deposits. The cross strata commonly contain chute-and-pool structures (Fig. 4a), drape large clasts with coarse lags deposited on their upstream side (Fig. 4b), truncate underlying strata (Fig. 4c,d), and form climbing dunes (Fig. 4d).

The most common occurrences of PH2 are dominated by alternating beds of matrix-supported, fine- to medium-grained ash with approximately 5–25% grains of coarse ash to fine lapilli; and clast-supported beds with <20% fine-

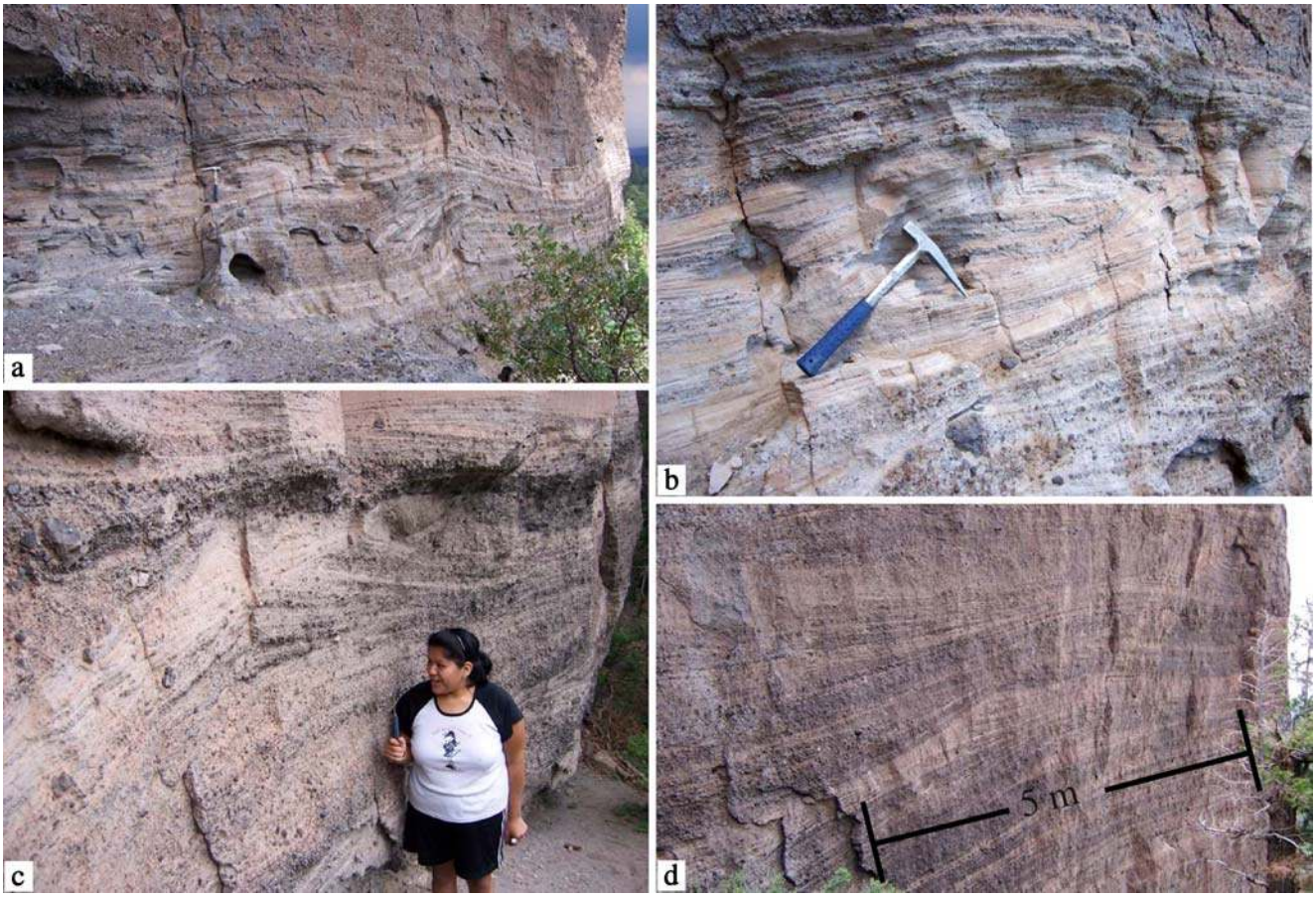

Fig. 4 PH2 as exposed in the first 20 m of the east–northeast measured section (location 3 in Fig. 1b). **a**, **b**, and **c** Fines-dominated, cross-stratified PH2 deposits described in the text (*hammer* for scale in **a** and **b**). **d** "Coarser-grained" PH2 deposits described in the text; the average grain size for these cross strata are fine to medium lapilli. Flow direction in all photographs is from *left* to *right*

grained ash matrix and ~80% grains of coarse ash to medium lapilli (Fig. 4a–c). Both of these bed types lack accretionary lapilli and exhibit minor soft-sediment deformation beneath larger ballistic clasts (typical sags are on the order of the size of the ballistic clast or smaller).

Coarser occurrences of PH2 are found on the east side of the outer crater (location 3, Figs. 1b and 4d), and consist of fairly well-sorted, reverse-graded beds from 0.2 to 2 m thick. The dominant grain size is typically fine to medium lapilli, and lenticular lags of coarse lapilli and fine blocks are common (5–10% fine blocks). Occasional coarser beds contain grains as large as coarse lapilli with some fine blocks. Clasts are ~90% accidental and ~10% juvenile (detailed below), and no sags are present beneath the larger clasts.

Three types of interbeds are common in PH2. The first are matrix-supported and exhibit faint planar and cross stratification, are composed of ~35% coarse ash to fine lapilli within ~65% fine-ash matrix, and vary in thickness from 5–30 cm. The second type of interbed is 2–4 cm thick and matrix-supported, with ~50% fine to medium ash matrix and ~50% coarse-ash-sized grains of primarily accidental material. The third interbed is typically 10–15 cm thick and clast-supported, with ~20% fine to medium ash matrix and ~80% coarse-ash-sized grains of primarily accidental material. Reverse grading is common in the second and third types of interbeds.

Juvenile clasts, including scoria and pumice, compose 20–75% of PH2. The compositions and percentages of juvenile and accidental lithics are described in detail in the clast analysis section below.

PH2 interpretation

Because of the cross-stratified nature of the deposits, we interpret PH2 to be a result of turbulent, dilute pyroclastic density currents, commonly known as *base surges* when they are associated with hydromagmatic eruptions (Fisher and Waters 1970; Schmincke et al. 1973; Allen 1982; Dellino et al. 1990; Cole 1991). Base surges have been previously characterized as either "wet" or "dry" depending on the evidence for liquid water in the deposits (Fisher and Waters 1970; Schmincke et al. 1973; Allen 1982; Dellino et al. 1990; Cole 1991). However, it can be problematic to distinguish antidune deposits that resulted from abundant liquid water at the time of deposition from those with little

to no liquid water, as these features can be formed either by dry, two-phase, critical to supercritical flow conditions; or by wet, three-phase cohesive flow conditions where grains are plastered on the upstream side of the dune (Fisher and Waters 1970; Schmincke et al. 1973; Allen 1982; Dellino et al. 1990; Cole 1991). PH2 lacks accretionary lapilli, pervasive soft-sediment deformation, and evidence of plastering or cohesive flows. Also, grain accretion occurs primarily on the lee side of dunes, which has been attributed to minor liquid water in the current (Schmincke et al. 1973; Allen 1982; Cole 1991). Therefore, we interpret PH2 to have been emplaced by dry, non-cohesive, two-phase (gas-particle) flows containing particles of varying density and size (Table 1).

Pyroclastic surges are density-stratified, dilute, turbulent flows (Fisher and Waters 1970; Crowe and Fisher 1973; Fisher 1979; Valentine 1987; Druitt 1992). As we have ruled out the presence of liquid water in the PH2 current, the long wavelengths and low-angle symmetrical dune to antidune, climbing-dune, and chute-and-pool structures found within the deposits are indicative of high flow energy, and are typically closely linked to high-velocity flows with Froude numbers (*Fr*) above 0.8 ($Fr = u/\sqrt{gh}$; where u = velocity, g = gravitational constant, and h = depth of flow; Jopling and Richardson 1966; Schmincke et al. 1973; Allen 1982; Valentine 1987; Cole 1991). In fluvial systems similar bedforms are related to upper-flow regime conditions undergoing traction deposition, but are the result of standing waves at the density interface, the free flow surface (Middleton 1965; Jopling and Richardson 1966; Barwis and Hayes 1985; Paola et al. 1989). In pyroclastic surges, symmetrical and antidune features are interpreted to be the result of standing internal waves developed within stratified flows (i.e., Valentine 1987; Druitt 1992), where dune migration is controlled by subcritical or supercritical flow conditions near the bed region (Valentine 1987). Thus, the relevant Froude number for pyroclastic surges (upstream dune migration when Fr > 1, downstream dune migration when $Fr<1$; Middleton 1965; Jopling and Richardson 1966; Barwis and Hayes 1985), is thought to be the ratio of flow velocity to internal gravity wave speed (Valentine 1987). It is written as $Fr = u/Ny_h$ (Lin and Pao 1979; Valentine 1987), where u = flow velocity, y_h = height scale, and N represents the maximum possible frequency of internal waves in a stratified flow ($N = \frac{1}{2\pi}\left(\frac{-g}{\rho}\frac{\mathrm{d}\rho}{\mathrm{d}y}\right)^{1/2}$; ρ = bulk density at a given height of the current and g = gravitational acceleration directed in the negative y direction; Lin and Pao 1979). The height scale, y_h, can be the height of an obstacle in the flow, or the depth through which a specified density difference occurs ($y_h = \frac{(\Delta\rho)_s d}{d\rho/d\eta}$, where $(\Delta\rho)_s$ = specified density difference; d = total flow thickness; ρ = surge bulk density; and η = dimensionless height y/d; Valentine 1987).

Hence, we interpret the deposits of PH2 to be the result of layer-by-layer deposition from a fully turbulent, dilute, density stratified current. The cross-stratified deposits imply that deposition from the bed load region would have been dominated by traction sedimentation. The first two interbeds described above pinch and swell laterally, and exhibit faint, thin cross-stratification; all of which suggests some degree of lateral transport. However, they also contain a high proportion of fine ash (65% fine ash in the first interbed, and 50% fine ash in the second), and have faint planar stratification. For these reasons, we suggest that they were deposited during the waning stages of a pyroclastic surge, reflecting both late-stage surge deposition (weak lateral transport) and co-surge ash fallout (planar-bedded fine ash). The coarse, grain-supported interbeds, which are commonly inversely graded, are interpreted to be the result of traction carpet sedimentation from a more concentrated basal region, which commonly occurs beneath turbulent flows (Lowe 1976, 1982; Postma 1986; Valentine 1987; Druitt 1992; Sohn 1997).

As with PH1, the abundant entrained accidental lithics and angular ash morphology indicate that fragmentation was dominantly driven by phreatomagmatic processes. However, the relatively high abundance (5–30%) of vesiculated juvenile material (20–60% vesicles) indicates that the magma was actively vesiculating prior to or simultaneously with water–magma interaction, and may suggest a second mechanism of fragmentation.

PH3: diffusely-stratified and reverse-graded pyroclastic deposits

PH3 is dominated by 0.5–2 m thick, laterally continuous, massive and planar beds with common interbeds of fine-grained cross strata (Fig. 5). PH3 commonly alternates and occasionally interfingers with the deposits of PH2 (Fig. 5d), and occurs wherever the coarse, clast-supported, massive third interbed of PH2 (described above) predominates over the cross-stratified tuffs and lapilli tuffs. PH3 beds are dominated by fine to coarse lapilli and <5% fine blocks within <20% fine ash to coarse ash matrix. Individual beds range from grain-supported to matrix-supported, commonly exhibit reverse grading and diffuse stratification, and pinch and swell laterally (Fig. 5a,b, and d). The coarser-grained, clast supported beds are fines-poor (lacking a significant fine-ash component of <30 μm in size). No accretionary lapilli were found. It is important to note that the proportion of bombs that show sags is greater in the deposits of PH3 than either PH2 or PH1 (Fig. 5c). However, the deformation is on the same scale as the other two FAs, with sag depth equal to or less than one ballistic clast diameter.

Clasts within PH3 are between 10–45% juvenile, including both scoria and pumice. The compositions and

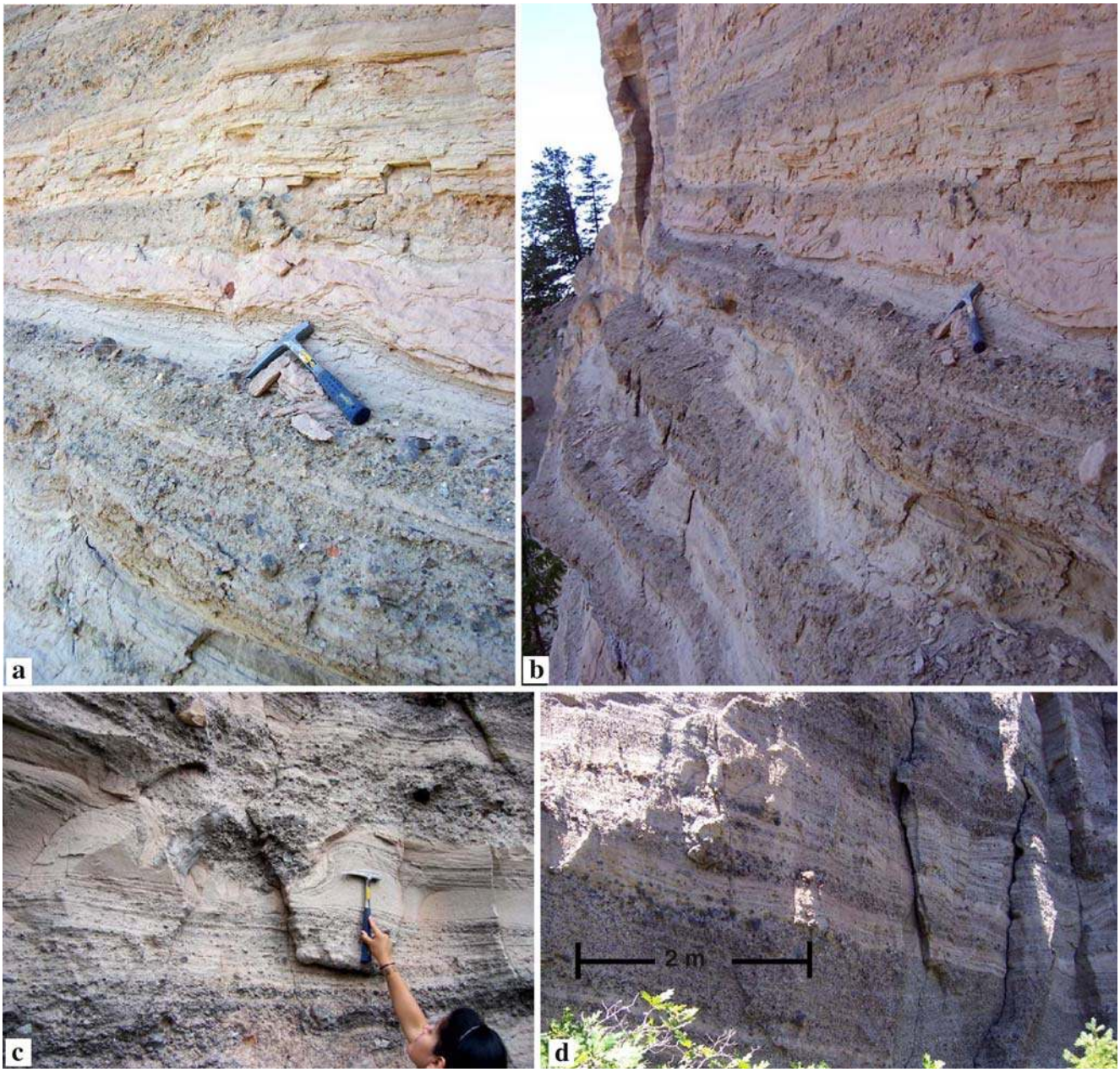

Fig. 5 **a**–**b** PH3 deposits as exposed in the west measured section (location 1 in Fig. 1b). **c**–**d** Photographs of PH3 deposits exposed in the east measured section (location 3 in Fig. 1b). **a**, **b**, and **d** Show the 0.5–2 m thick, laterally continuous deposits of massive and planar beds with common interbeds of fine-grained cross strata; **c** indicates the scale of soft-sediment deformation associated with ballistic or large clasts

percentages of juvenile and accidental lithics are described in detail in the clast analysis section below.

PH3 interpretation

Sedimentary characteristics vary among the beds. This suggests that the dominant transport and depositional mechanisms of PH3 varied with each explosive pulse, producing unique particle concentrations, grain sizes, velocities, and flow conditions for each density current. The massive, poorly sorted, fines-rich deposits that lack grading are suggestive of rapid deposition from high-concentration suspensions with little tractional transport (Sohn and Chough 1989; Chough and Sohn 1990; Fisher and Schmincke 1994). However, the dominant bedding characteristics within PH3 are diffusely stratified, coarse-grained, grain supported, and commonly inversely graded deposits capped by, or interbedded with, fine-grained, matrix-supported, cross-stratified deposits. We interpret these deposits to be the consequence of traction carpet

flow conditions beneath a high-density, turbulent current (Lowe 1976; Lowe 1982; Sohn 1997).

Traction carpets are hypothesized to have two main regions; a lower, viscous and slow moving region dominated by granular flow within the frictional regime (traction carpet), and an upper, less viscous and less concentrated, fast moving region dominated by turbulence (Lowe 1982; Hanes and Bowen 1985). Massive to diffusely stratified deposits exhibiting reverse grading are often attributed to the lower viscous regions where zones of high shear rates and high dispersive pressure occur (Chough and Sohn 1990; Branney and Kokelaar 1992, 2002; Sohn 1997). These features could also result from temporal variations in clast size as the deposit aggrades, or from waxing and waning of the flow (Kneller and Branney 1995). The pinch-and-swell features, interfingering of finer-grained cross-bedded deposits, diffuse stratification, and splay-and-fade features all suggest that turbulence was also an important transport mechanism (Valentine 1987; Chough and Sohn 1990; Branney and Kokelaar 1992).

The three controls on traction carpet thickness are applied shear stress, grain flux rate, and grain size (Sohn 1997). The thickness of a traction carpet is dependent on the supply rate of sediment from the overlying flow and the deposition rate at the base of the traction carpet (Lowe 1976; Drake 1990; Sohn 1997). Lowe (1976) explains that the sediment supply rate is a function of particle concentration and capacity of the overlying flow, whereas the deposition rate is a function of grain size because the base of a high-concentration granular fluid is most strongly affected by particle settling velocity. Hence variations in PH3 deposit characteristics and thickness from one bed to another are interpreted as a result of varying initial particle concentrations, particle settling rate, and flow conditions from each eruptive pulse.

PH3 contains only occasional evidence of soft-sediment deformation and lacks accretionary lapilli, which suggest that liquid water was not abundant during emplacement. However, the proportion of ballistic clasts with accompanying sags is greater in PH3 than in PH1 and PH2. This suggests that during intervals when PH3 dominated, liquid water was more abundant in the pyroclastic currents.

As with PH1 and PH2, the presence of vesiculated juvenile material (20–60% vesicles), along with abundant entrained accidental lithics and angular ash morphology, indicate that fragmentation was dominated by phreatomagmatic processes, but that fragmentation due to magmatic exsolution may have also occurred.

M1: minette lava flows

The NPM pyroclastic sequence is overlain by three minette lava flows (stratigraphically labeled Tva, Tvb, and Tvc by Ehrenberg 1978; Fig. 6). Tva is an extrusive minette with phenocrysts of olivine, clinopyroxene, and phlogopite 1–3 mm in diameter in an aphanitic groundmass. Tvb is compositionally identical to Tva, but is a coarser-grained lava with a groundmass of sanidine crystals 0.5–1 mm in diameter that poikilitically enclose the ferromagnesian minerals (Ehrenberg 1978). Tvc, the youngest unit, is an aphanitic, greenish-grey felsic minette lava with phenocrysts of phlogopite and diopside in a trachytic groundmass of feldspar laths (Ehrenberg 1978). Tvc is more evolved than Tva and Tvb, and exhibits bands and marbling that may indicate magma mixing. Upon eruption, Tvc carried abundant nodules of spinel peridotite and subordinate websterite and granulite; most xenoliths near the surface of the flow were subsequently altered and eroded, leaving voids. Remnant xenoliths now compose about 5% by volume of Tvc exposed in outcrops (Ehrenberg 1978).

M1 interpretation

M1 lava flows have a sharp contact with the pyroclastic deposits from the phreatomagmatic stage of the eruption. There were no signs of the groundwater being gradually depleted or isolated from the vent, as seen within other phreatomagmatic-pyroclastic sequences where tephra deposits grade into strombolian cinder deposits, and finally into lava flows (e.g., Sohn and Chough 1989; Houghton et al. 1999; Brand and White 2007). Instead, at NPM there seems to have been an abrupt transition from phreatomagmatic to effusive activity. No paleosols or obvious signs of surface alteration or erosion were found between the pyroclastic and effusive deposits. In some areas the lava flows intrude the crater walls at the pyroclastic-lava contact, indicating that the tuffs were not lithified at the time of the effusive stage. Within the crater, the lava flows are slightly pillowed in some places, which suggests that water may have ponded in the crater before the effusive stage (Fig. 6c). Similar features have been observed within the crater of South Alkali Butte (Lucero Volcanic Field, New Mexico), where pillowed lavas locally intrude down into the underlying deposits (Valentine and Groves 1996). Finally, the Tva and Tvb mafic minette lavas have the same phenocryst assemblage as the juvenile scoriaceous clasts found in the phreatomagmatic deposits, indicating that the first lavas erupted were no more or less evolved than the minette magma involved in the prior phreatomagmatic stage. Although there might have been a short repose period between the pyroclastic and effusive stages of the eruption, the repose was not long enough to allow an erosional horizon or paleosol to form.

M2: minette plugs and dikes

Two plugs of aphanitic mafic minette and one cluster of dikes and scoriaceous rubble also occur within the crater at

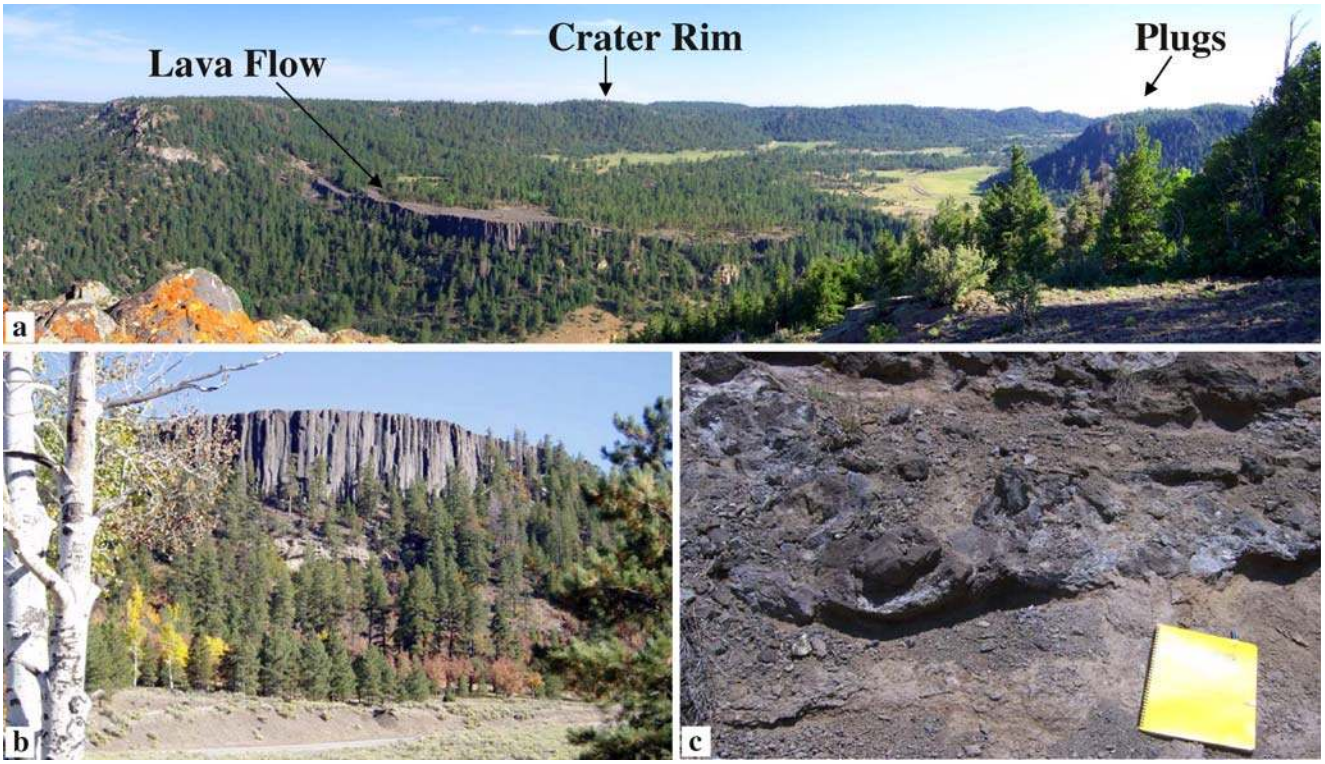

Fig. 6 Minette lava flows and plugs of M1 and M2. **a** View north–northeast across the NPM crater (~1.5 km diameter) from atop the west measured section (location 1 in Fig. 1b). Columnar-jointed lava flows seen in the *middle-left part* of the photograph follow topography up and over the rim, possibly indicative of post-crater subsidence. The hills to the right are M2 plugs. **b** M1 (Tva in Fig. 1c) flow (~10 m thick) viewed from the crater floor. **c** Contact between the M1 flow and underlying pyroclastic deposits within the crater. This photograph displays the pillow features indicative of water ponded in the crater prior to emplacement of the lava flow (21.6×28 cm notebook for scale)

NPM (Figs. 1b, 6a and b; labeled Ti by Ehrenberg 1978). The plugs have columnar jointing and are generally nonvesicular, except in their uppermost parts. This nonvesicular mafic minette is petrographically and compositionally similar to the oldest lava, Tva (Ehrenberg 1978).

M2 interpretation

It is not clear whether the plugs and dike cluster mark the location of the vent or vent focus during either the phreatomagmatic or the effusive stage. Ehrenberg (1978) identified these as intrusive bodies that were exhumed during post-eruptive subsidence of the maar crater. However, based on their aphanitic textures and topographic position above the lava flows, we interpret these plugs as dome-like features that emerged in the crater during the effusive stage.

Clast analysis

We estimated the type and percentage of accidental and juvenile clasts for all measured sections. Grain type and percentage were estimated in the field for grains larger than coarse ash, as finer grains were too small to accurately identify in hand sample (Table 3). Clasts larger than coarse ash include mudstone and sandstone, accidental minette, juvenile magma, and crystalline mantle and lower-crustal xenoliths (Table 3). The matrix was defined as the proportion of each unit finer than coarse ash, and its composition was analyzed petrographically as described below. Cumulative proportions of individual components were calculated by combining field and petrographic estimates.

The white sandstone and unconsolidated rounded quartz sand grains were determined to have originated from the underlying Narbona Pass Member of the Chuska Sandstone. They are of the same composition, grain size, rounding, and sorting (relative to the other sand grains) as those of the Narbona Pass Member as sampled immediately below the maar deposits. These grain characteristics do not correspond to any of the other sedimentary units below the maar (based on outcrops throughout the region). In addition, the disaggregated sand grains likely originated from the more friable sections of the Narbona Pass Member, whereas the (rare) consolidated sandstone likely originated from more indurated sections. It is difficult to ascertain the stratigraphic origin of the other accidental sedimentary clasts, as the exact stratigraphy below the Narbona Pass Member is not well constrained. Both the mudstone and arkosic-argillaceous white sandstone are consistent with descriptions of the Deza Member from the

Table 3 Description of clasts (both accidental and juvenile) identified in hand sample from all measured sections at NPM and corresponding source units, identified from the well-documented regional stratigraphy (Wright 1956; Trevena and Nash 1979; Lucas and Cather 2003)

Clast name	Accidental/ juvenile	Description-distinguishing characteristics	Source unit
Mudstone	Accidental	White-to-gray mudstone containing thin (<5 mm) lenses of silty-fine sand layers. It is both laminated and massive	Deza Member of the Chuska Sandstone
Dirty white sandstone	Accidental	Fine-grained sandstone which consists of subangular to subrounded grains	Deza Member of the Chuska Sandstone
Red sandstone	Accidental	Fine-grained, well sorted red sandstone. Clasts appear generally massive, but occasionally exhibit bedding	Mesozoic Strata
Purple sandstone	Accidental	Fine-grained, massive, purple sandstone	Mesozoic Strata
White sandstone/ sand grains	Accidental	Well sorted, fine-grained sandstone consisting of subrounded to rounded quartz sand with minor amounts of heavy minerals. Individual fine-to-medium, well rounded quartz sand grains were commonly identified in the matrix of the pyroclastic rocks	Narbona Pass Member of the Chuska Sandstone
Angular minette	Accidental	Dense, angular, non-glassy, non-vesicular accidental minette	Hypabyssal intrusions of minette magma, solidified prior to NPM phreatomagmatic eruption
Pumice	Juvenile	Irregular, sometimes flattened, finely vesiculated, sometimes highly altered pumice, ranging in color from white to gray to brown. They range in size from <5 mm to 30 cm, and often contain >1 mm sized biotite-phlogopite minerals	They are interpreted to be juvenile pumice because of their compositional similarity to juvenile ash, and the degree of vesiculation
Scoriaceous minette	Juvenile	Dark, irregularly-shaped scoriaceous clasts. They are frequently found flattened, often have quenched rinds, and occasionally contain inclusions of mudstone and/or sandy mudstone	Juvenile scoria
Crystalline mantle and deep crustal granitic xenoliths	Accidental	~2–5% of each outcrop contains xenoliths of Peridotite, granite, and gneiss, which appear to be derived from the mantle and are not related to the phreatomagmatic accidental clasts	Crustal and mantle xenoliths

Crystal Creek outcrop several kilometers to the west and other localities (Wright 1956; Lucas and Cather 2003). The red and purple sandstone likely originated from the older Mesozoic sandstone units, which crop out just west of NPM.

Distinguishing between accidental minette lithics and juvenile clasts in the field is challenging. Accidental minette was generally angular, exhibited evidence of abrasion during transport, and lacked features typical of juvenile dense blocky lapilli (e.g., platy slabs bounded by curvi-planar fracture surfaces, fluidal contorted slabs, or gnarled, bread-crusted, or cauliflower surfaces; Houghton et al. 1999). The accidental minette lithics are interpreted to have originated from previously solidified dikes and sills beneath NPM, and will be referred to as hypabyssal minette.

The scoriaceous juvenile minette clasts are distinct from the hypabyssal minette in that they display quenched rinds; are irregular, splotchy, or twisted-fluidal in shape; sometimes show breadcrusted or cauliflower surfaces; and often incorporate pieces of sand, or show mixing with a sand-mud slurry. The occasional presence of wall rock grains in some of the juvenile clasts suggests that magma interacted with water-bearing wall rocks prior to fragmentation (e.g., Schmincke 1977; Houghton and Schmincke 1986; Houghton et al. 1999). More conclusive evidence for the distinction between hypabyssal versus juvenile minette is presented below in the thin-section analyses. The pumiceous lapilli clasts found in the section were difficult to identify in the field because of heavy alteration. However, subsequent thin-section analysis also verified that these are juvenile clasts of finely-vesiculated minette pumice from the erupting magma, as they have phenocryst assemblages identical to those of the juvenile minette.

Crystalline mantle and lower-crustal xenoliths were also identified within the pyroclastic rocks, and compose a consistent 1–3% of the clasts. Rock types observed include spinel peridotite, websterite, granite, and granulite.

Thin-section analysis

Twenty-six thin sections from multiple lithofacies within all measured sections were analyzed and point-counted to better constrain the composition and percentage of accidental versus juvenile clasts, especially in the matrix. For

each thin section, 300 points were counted with ~1 mm spacing between traverses and between points. One juvenile and ten accidental clasts were identified (Table 4; see Supplemental online material for a more detailed petrographic description). More accidental sedimentary lithics were identified in thin section than in hand sample, which indicates that they were either present only as grains too small to identify, or were too similar to distinguish in hand sample. The relative abundances and the importance of these lithics are discussed in the next section.

The accidental volcanic lithics (C1, grey mafic; C2, minette) in thin section correspond to the hypabyssal minette identified in hand sample. They are dominantly angular, but some clasts are slightly abraded and rounded, have a crystalline groundmass, and contain partially melted rounded quartz siltstone clasts. The partial melting of the siltstone strongly suggests that it was in contact with minette magma for an extended period prior to cooling. This supports the idea that the host minette originated as an intrusion that entrained sedimentary lithics during ascent, prior to the phreatomagmatic event. The crystalline groundmass also suggests a slower cooling rate. Finally, the angularity and occasional abrasion of the clasts suggest that they were entrained during the phreatomagmatic phase, and subsequently transported within eruption columns or density currents.

J1 is interpreted to be a juvenile clast because of its irregular shape; quenched, glassy groundmass; glassy rinds; vesiculated texture; and entrained, accidental quartz sand grains. Its phenocryst assemblage indicates that it is similar in composition to the Tva and Tvb minette lavas. The varying degrees of vesicularity (20–60%) suggest that magmatic vesiculation occurred prior to or simultaneously with fragmentation, and that while hydromagmatic fragmentation was dominant, some simultaneous fragmentation due to exsolution of magmatic volatiles may also have occurred (Houghton and Wilson 1989; Houghton et al. 1999; Cole et al. 2001). The sand grains within the glass matrix are evidence for mixing between the intruding magma and the disaggregated Narbona Pass Member found in the pyroclastic matrix.

Facies association and clast distribution

Three outer-crater stratigraphic sections (Figs. 7, 8 and 9) illustrate the distribution of FAs and lithics around the volcanic edifice. Field estimates of grain type and percentage are compared to thin-section analyses of matrix composition for various elevations throughout the stratigraphy around the vent (Figs. 7, 8 and 9; Tables 5 and 6). Table 5 shows field estimates of percent matrix, as well as lithic abundances normalized to the non-matrix portion of the unit. Throughout each section, the dominant accidental material from subsurface sedimentary units are disaggregated sand grains from the Narbona Pass Member (17–50%), red Mesozoic sandstone (0–20%), and minor amounts of purple Mesozoic sandstone, greywacke, and mudstone. The thin-section analyses reveal additional siltstones and micrites, likely derived from either the Deza Member of the Chuska Sandstone, or the Upper Cretaceous Mancos Shale, which is exposed immediately beneath the Chuska Sandstone west of NPM. Accidental material from the sedimentary units underlying the Chuska Sandstone do not occur as disaggregated particles in the matrix, but only as larger clasts.

The relative abundances of the sedimentary lithics derived from below the Narbona Pass Member remain constant throughout the entire pyroclastic section. That is, accidental clasts of red sandstone, purple sandstone, greywacke and mudstone–siltstone do not vary in relative proportions of one to the other, which allows them to be broadly grouped together as non-Narbona Pass Member accidentals. Therefore, clast abundances are reported as relative proportions of Narbona Pass Member accidentals, non-Narbona Pass Member accidentals, hypabyssal minette, and juvenile material (Figs. 7, 8 and 9; Tables 5 and 6).

The vesicles within the fine ash tuff matrix were examined in thin section and constitute three size classes.

Table 4 Clast types identified in thin sections (detailed descriptions of these clasts are available as online supplemental material)

Clast name	Accidental/juvenile	Subsurface unit
C1—gray mafic	Accidental	Hypabyssal minette
C2—minette	Accidental	Hypabyssal minette
Fine-medium grained sandstone (S1)	Accidental	Narbona Pass Member, Chuska Sandstone
Individual rounded quartz sand grains	Accidental	Narbona Pass Member, Chuska Sandstone
Dirty sandstone (S2)	Accidental	Non-Narbona Pass Member
Quartz siltstone	Accidental	Non-Narbona Pass Member
Silty micrite	Accidental	Non-Narbona Pass Member
Silty mudstone	Accidental	Non-Narbona Pass Member
J1	Juvenile Pumice/Scoria	Juvenile minette magma

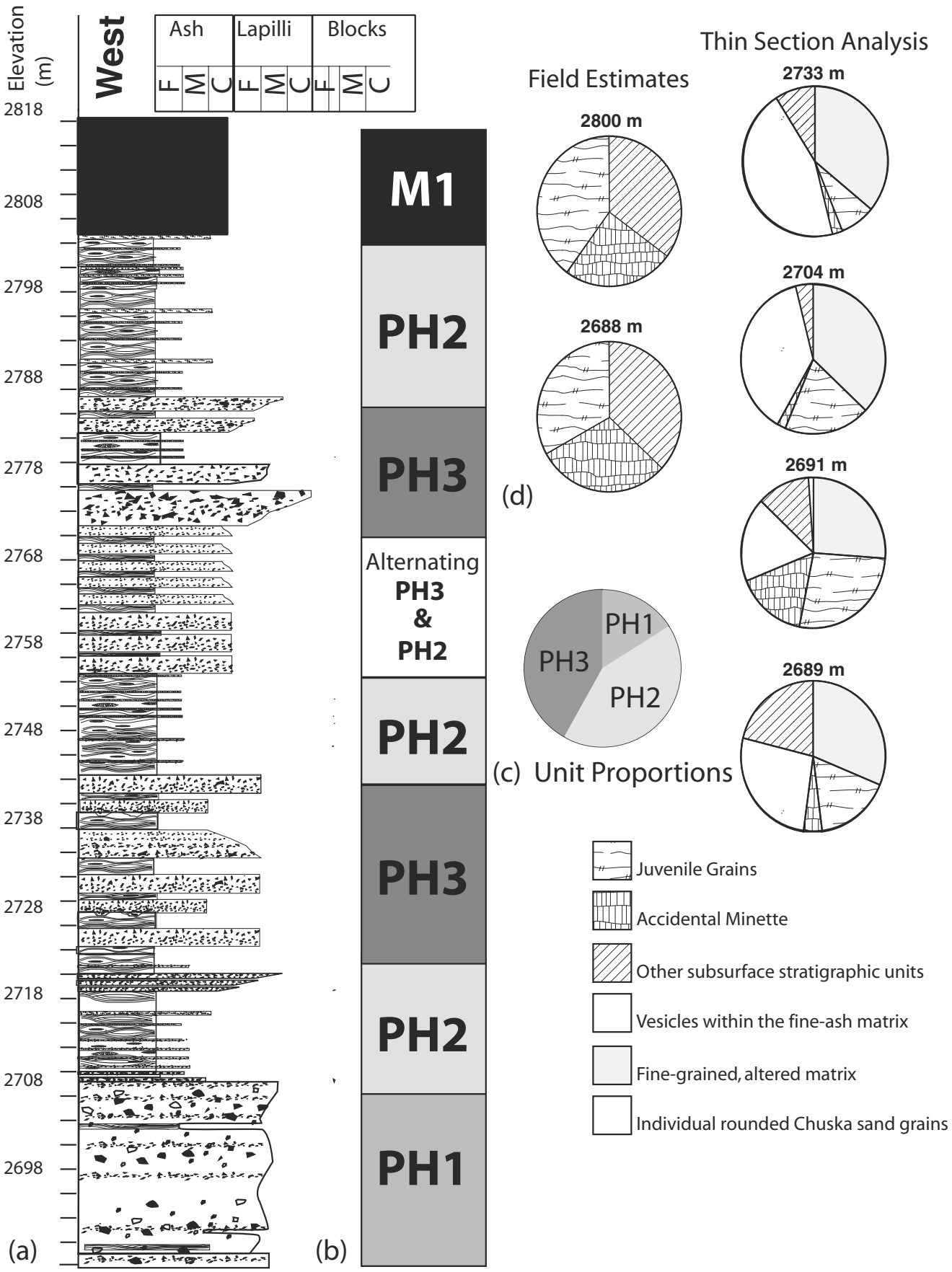
Elevation (m)
West
Ash
Lapilli
Blocks
F M C
2818
2808
2798
2788
2778
2768
2758
2748
2738
2728
2718
2708
2698
(a)
M1
PH2
PH3
Alternating PH3 & PH2
PH2
PH3
PH2
PH1
(b)
Field Estimates
2800 m
2688 m
(d)
Thin Section Analysis
2733 m
2704 m
2691 m
2689 m
PH1
PH3
PH2
(c) Unit Proportions
Juvenile Grains
Accidental Minette
Other subsurface stratigraphic units
Vesicles within the fine-ash matrix
Fine-grained, altered matrix
Individual rounded Chuska sand grains

◀ **Fig. 7** **a** Stratigraphic column representing the deposits on the western side of the volcanic edifice. **b** Generalized stratigraphic column showing facies associations. **c** Relative proportions of units in this section. **d** Relative proportions of accidental lithics and juvenile material estimated in the field (*left column*) and by thin-section analysis (*right column*). Vesicles within the fine-ash matrix show the relative area taken up by the vesicles themselves, not the amount of fine ash matrix that was vesiculated

The smaller vesicles (100–600 μm) have a semicircular cross section, the medium sized vesicles (600 μm–2 mm) are rounded to irregular in shape, and the largest vesicles (4–5 mm, rare) are highly irregular in shape. Most vesicles are small to medium in size. The vesicles show no preferred orientation and are not stretched. Many vesicles are filled

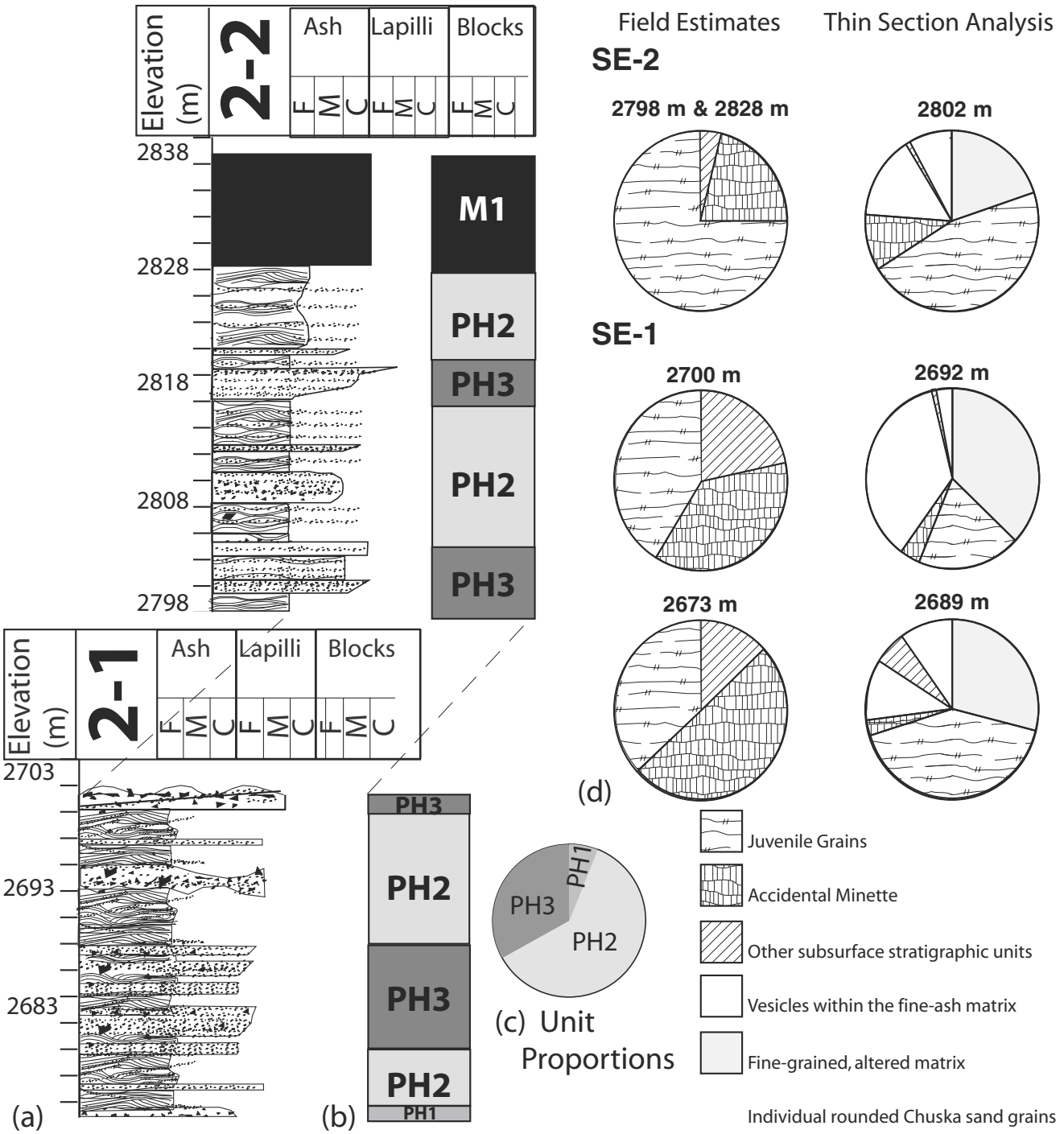

Fig. 8 **a** Stratigraphic column representing the deposits on the southeast side of the volcanic edifice. **b** Generalized stratigraphic column showing facies associations. **c** Relative proportions of units in this section. **d** Relative proportions of accidental lithics and juvenile material estimated in the field (*left column*) and by thin-section analysis (*right column*)

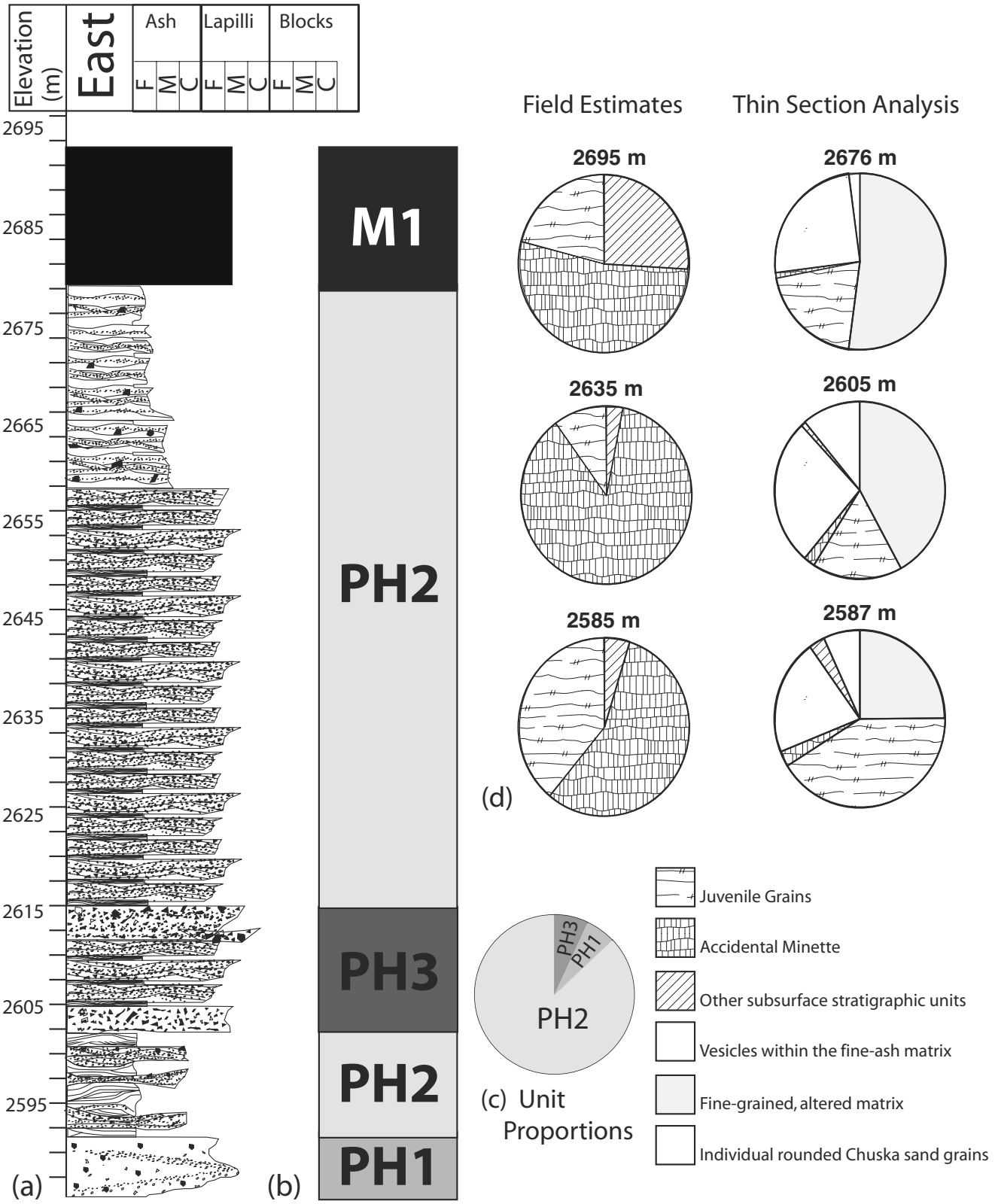

Fig. 9 **a** Stratigraphic column representing the deposits on the eastern side of the volcanic edifice. **b** Generalized stratigraphic column showing facies associations. **c** Relative proportions of units in this section. **d** Relative proportions of accidental lithics and juvenile material estimated in the field (*left column*) and thin-section analysis (*right column*)

Table 5 Field estimates of grain type and abundance with location around vent

Grain types-field estimates	West (%)		Southeast-1 (%)		Southeast-2 (%)	East (%)		
	2,688 m	2,800 m	2,673 m	2,700 m	2,828 m	2,585 m	2,635 m	2,695 m
Narbona Pass Member, Chuska	3	6	4	5	–	–	–	8
Non-Narbona Pass Member lithics	37	34	11	20	7	7	5	19
Hypabyssal Minette	30	24	48	37	21	56	87	53
Juvenile pumiceous ash clasts	28	36	30	23	72	37	8	20
Juvenile Scoria	2	–	7	15	–	–	–	–
Fine-grained Matrix	60	60	35	25	70	60	10	40

The clast proportions were normalized to the non-matrix portion. The percent matrix generally reflects the proportion of fine-grained material present at each location. The sandstone from the Narbona Pass Member does not include disaggregated sand grains. The "non-Narbona Pass Member" groups all other sedimentary clasts (mudstone, siltstone, and dirty white, purple, and red sandstones), and includes mantle and crustal xenoliths.

with a black gritty secondary material, or have been subsequently filled with calcite crystals.

West tuff ring

The measured west section (location 1 in Fig. 1b) begins at 2,688 m elevation, and the contact with the Chuska Sandstone is exposed approximately 10 m downsection. The base of the west section consists of approximately 20 m of poorly sorted, massive PH1 (Fig. 7), above which there is an abrupt transition into alternating sequences of PH2 and PH3. The section between 2,757 and 2,770 m is unique in that it has uniformly alternating 0.5–1 m thick beds of PH2 and PH3. Above this the section is dominated by PH3, followed by the fine-grained deposits of PH2. The contact between PH2 and M1 lava is sharp, showing no evidence of erosion or paleosols (Fig. 7).

Bomb sags are more numerous within this section than in the southeast and east–northeast measured sections. The vertical extent of each sag is comparable to the ballistic clast diameter. No accretionary or armored lapilli were found.

The lithic types and abundances estimated in the field do not change significantly throughout the west section (Fig. 7d). Subequal proportions of juvenile grains, hypabyssal minette, and accidental subsurface sedimentary units are consistent from the base to the top (Table 5).

The thin-section analysis demonstrates that while the amount of indurated Chuska Sandstone is low relative to other accidental clasts in hand sample, it is abundant in the matrix as disaggregated, subrounded to rounded sand grains (between 17–38%; Table 6). The percentage of Narbona Pass Member sand grains in the matrix increases up section (up to 38%), while the proportions of other accidental sedimentary-derived grains and juvenile grains decrease (non-Narbona Pass Member from 12% to 4%, and the juvenile grains from 27% to 19%). The uppermost thin section was collected at an elevation of 2,734 m; however, field analysis confirmed that the matrix in the highest part of the west section (2,799 m) composes an estimated 60% of the sample, while hand-lens inspection showed that the matrix was dominated by rounded quartz sand grains and fine-to-medium grained ash.

Cumulative proportions of each component were calculated by combining field estimates and thin-section point counts. In the west, juvenile material (juvenile clasts plus fine ash) predominates at roughly 45%, while disaggregated grains of the Chuska Sandstone compose nearly 30%.

Table 6 Thin-section analysis of grain type and abundance in matrix

Thin section analysis	West (%)				SE-1 (%)		SE-2 (%)	East (%)		
	2,689 m	2,691 m	2,704 m	2,733 m	2,689 m	2,692 m	2,802 m	2,587 m	2,605 m	2,676 m
Narbona Pass Member	17	18	38	45	11	36	15	21	27	25
Non-Narbona Pass Member	2	12	4	9	6	1	1	3	1	–
Hypabyssal Minette (C1, C2)	16	16	2	2	3	4	10	3	2	1
Juvenile Grains	22	27	19	8	41	19	46	41	17	20
Altered, fine ash matrix	31	26	37	36	29	37	20	25	42	52
Vesicles within matrix	12	1	–	–	10	3	8	7	11	2

Narbona Pass Member includes disaggregated and indurated sandstone/sand grains, but is dominated in all sections by individual sand grains. "Non-Narbona Pass Member" lithics include all other sedimentary clasts (mudstone, siltstone, and dirty white, purple, red sandstones, and mantle/deep crustal xenoliths). Juvenile grains include both pumiceous and scoriaceous material for the thin-section analysis.

Minor proportions of non-Narbona Pass Member sedimentary units (15%) and hypabyssal minette (10%) make up the rest of the unit. All cumulative proportions remain nearly constant from the base to the top of the western section.

Southeast tuff ring

The southeast measured section (location 2–1 in Fig. 1b) begins at an elevation of 2,673 m. The base of the section is not exposed here. The basal deposits at this section are approximately 2 m of poorly sorted, massive PH1, with a sharp upward transition to alternating sequences of PH2 and PH3 (Fig. 8). The exposure at this location ends at 2,703 m elevation, but the measured section is continued 0.5 km to the south (location 2–2 in Fig. 1b) at an elevation of 2,798 m. PH2 and PH3 dominate this part of the section. M1 lavas directly overlie the top of the pyroclastic section. The oldest flow, Tva, locally intrudes the uppermost part of the tuff ring, indicating that the phreatomagmatic deposits in the tuff ring were not lithified at the time of M1 extrusion.

Bomb sags (again scaling with bomb size) occur beneath some, but not all, ballistic clasts in this section. No accretionary or armored lapilli were found.

Our estimates in the field indicate that at its base, the southeast section contains a high proportion of hypabyssal minette and juvenile grains; most of the latter are pumiceous ash clasts (Fig. 8d; Table 5). Several tens of meters up section (at ~2,700 m), the percentage of hypabyssal minette decreases, the percentage of sedimentary-derived (both Narbona Pass Member and non-Narbona Pass Member) accidental clasts increases, and the percentage of juvenile grains remains approximately constant. Towards the top of the southeast section (at locality 2–2 in Fig. 1b), juvenile clasts increase to nearly 75%, while sedimentary-derived accidental clasts and hypabyssal minette decrease to less than 25%.

Thin sections of the matrix of the units in the southeast measured section reveal that the base of the section contains a high percentage of juvenile grains (~41%) and a relatively low percentage of individual sand grains (~11%). However, a few meters up section, individual sand grains increase to 36% as juvenile grains decrease to 19%, consistent with the field estimates. Toward the top of the southeast section, the juvenile grains again increase (up to 46%) and individual sand grains decrease (15%).

Calculations of cumulative proportions reveal that the southeastern section is dominated by juvenile material (juvenile clasts plus fine ash) which, beginning a few tens of meters above the base, increases gradually up-section from 45% to 75%. The proportion of hypabyssal minette is also significant, decreasing from >30% at the base to just under 20% at the top of the section. Sedimentary clasts are minor in the southeast, with Narbona Pass Member and non-Narbona Pass Member components each composing less than 10% of the unit. Units sampled from the southeastern side of NPM contain a higher percentage of juvenile grains and hypabyssal minette, and a lower percentage of Narbona Pass Member sand grains than those sampled from the western side.

East–northeast tuff ring

The east–northeast measured section (location 3 in Fig. 1b) begins at 2,585 m elevation, about 5 m up section from the contact between the pyroclastic deposits and the Narbona Pass Member. This measured section begins at a lower elevation than the other sections do, because the pyroclastic deposits here fill a paleovalley in the Chuska Sandstone (Appledorn and Wright 1957). The base of the section consists of 5 m of poorly sorted, massive PH1, then a sharp upward transition to an alternating sequence of PH2 and PH3 (Fig. 9). The first 10 m of PH2 is fine-grained (fine ash to medium lapilli), matrix-supported, exhibits cross strata with grains of coarse ash to fine lapilli, and contains coarse, massive, reversely graded interbeds similar to PH3. The next ~40 m of section is coarser-grained PH2 (grain sizes up to coarse lapilli and fine blocks) and contains low-angle duneforms with wavelengths from 3–5 m and amplitudes of one meter or less (Fig. 4d). Above 2,659 m elevation, PH2 is again dominated by finer-grained deposits (fine ash to medium lapilli) and continues to the top of the section. The contact between the pyroclastic sequence and M1 lavas is sharp and shows no paleosols or obvious erosional horizons.

In the first 18 m of this section (below the coarse PH2 deposits), bomb sags are present at the same abundance as in the southeast measured section. As in the other sections, deformation scales with the size of the ballistic clast. However, in the coarse PH2 deposits no soft-sediment deformation was recognized. In the fine PH2 deposits above 2,657 m elevation, bomb sags are again observed, but they are far less abundant than at the bottom of the section. No accretionary or armored lapilli were found.

At the base of the east–northeast section, field estimates of grain type and percentage indicate subequal proportions of hypabyssal minette clasts and juvenile grains, and <5% sedimentary-derived accidental grains (Fig. 9d; Table 5). However, at 2,605 m, where the coarser-grained PH2 appears, the abundance of hypabyssal minette component increases to >85%, with juvenile grains comprising <8%, and accidental sedimentary clasts comprising <3%. At the top of the section the percentage of hypabyssal minette again decreases to ~53%, while sedimentary-derived accidental clasts and juvenile material increase to subequal proportions (19–20%; Table 5).

Thin-section analyses of the east-northeast section show a relatively consistent proportion of individual Narbona

Pass Member sand grains throughout the section (21–27%), and an overall decrease in the proportion of juvenile grains from 41% at the base, to 17% in the middle, and to 20% at the top, which is consistent with field estimates (Fig. 9d; Table 6). The decrease in juvenile grains corresponds to an increase in the fine ash matrix. The spike in the amount of hypabyssal minette in the middle part of the section is not reflected in the matrix.

Juvenile material (juvenile clasts plus fine ash) dominates the cumulative proportions at the base and the top of this section (50–60%), with hypabyssal minette also reasonably abundant (25–30%). The center of the section, as also noted by field estimates, is dominated by hypabyssal minette (80%), while juvenile material makes up 20% of the unit. As in the southeast, sedimentary clasts are minor throughout the section, typically composing 5–10% of the unit, with Narbona Pass Member grains occasionally composing up to 15%.

Discussion

The first eruptive products from NPM were the massive, concentrated pyroclastic density current deposits of PH1, consistent with the observation that maar volcanoes often produce massive lapilli tuff or tuff breccias during an initial vent-clearing phase (Wohletz and Sheridan 1979; Godchaux et al. 1992). After PH1, the stratigraphy is dominated by alternating sequences of PH2 and PH3, which have been interpreted as products of dilute density currents (PH2), and more concentrated density currents dominated by traction carpet flow conditions (PH3). The deposits of PH2 and PH3 are well-stratified and periodic, reflecting the pulsating nature of this eruption. Little to no evidence for the presence of liquid water during deposition was found throughout the section, and the proportion of juvenile material fluctuated only slightly (variations generally of less than 20%). This suggests that the eruptive conditions, such as the influence of external water, fragmentation efficiency, and eruptive energy, did not vary significantly during this eruption.

The final stage of the NPM eruption produced lava flows and plugs. Minette lava flows directly overlie the pyroclastic deposits, and in some places intrude parts of the upper tuff ring walls. This indicates that there was no explosive magmatic (e.g., Strombolian) phase between the phreatomagmatic and effusive phases. No erosional horizons or paleosols were observed at these contacts. However, the pillowed lava-flow features inside the crater suggest that water ponded locally and immediately prior to the effusive stage of the eruption (also noted at the Lucero volcanic field by Valentine and Groves 1996). Thus, although there was probably some pause between the phreatomagmatic and effusive stages, it was geologically brief.

"Wet" and "dry" are commonly used qualitative descriptions of phreatomagmatic eruptive conditions, based on deposit characteristics (Sohn and Chough 1989; Büttner et al. 1999; Nemeth et al. 2001; White 2001; Cole et al. 2001; Brand and White 2007). Wet conditions are typically indicated by a combination of features such as accretionary lapilli, fine-grained vesiculated tuff, pervasive soft-sediment deformation, surge cross-strata with stoss-side accretion and evidence for plastering, mud cracks, debris-flow filled erosion channels, and lahar deposits (Waters and Fisher 1971; Lorenz 1974; Wohletz and Sheridan 1979; Dellino et al. 1990; Sohn and Chough 1989; Nemeth et al. 2001; White 2001; Cole et al. 2001; Brand and White 2007). Wet-phreatomagmatic conditions are interpreted to occur when external water at the zone of magma–water interaction is not efficiently converted to steam (Sheridan and Wohletz 1983; Wohletz and McQueen 1984), and abundant liquid water is retained in the eruption column and density currents.

Dry conditions are indicated by juvenile material largely present as highly fragmented fine to coarse ash (although this occurs in wet conditions as well), low-angle cross strata with dominantly lee-side accretion, no evidence of accretionary lapilli, and little to no soft-sediment deformation (e.g., Fisher and Waters 1970; Sheridan and Wohletz 1983; Sohn and Chough 1989; Nemeth et al. 2001; Doubik and Hill 1999; Chough and Sohn 1990; Brand and White 2007). Dry-phreatomagmatic conditions represent efficient conversion of external water to steam at the site of magma–water interaction, or subsequently in the eruption plume. As a consequence, little or no liquid water is retained in the eruption column or proximal density currents, although steam may condense in density currents and rising plumes farther from the source (e.g., Sheridan and Wohletz 1983; Wohletz and McQueen 1984). These conditions are thought to represent highly efficient conversion of thermal energy to kinetic energy, yielding the highest degree of melt fragmentation and therefore the highest explosivity (Wohletz and McQueen 1984; Büttner and Zimanowski 1998).

At NPM we found no accretionary lapilli, and while bomb sags were observed in some areas, they were about equal in size to the ballistic clasts that formed them. This scale of deformation is minor compared to that observed in deposits interpreted as originating from wet-phreatomagmatic eruptions such as Tihany (Pannonian Basin), Hungary (Nemeth et al. 2001); Pahvant Butte, Utah (White 2001); Sinker Butte Tuff Cone, Idaho (Brand and White 2007); and the 1957–1958 Capelinhos eruption, Faial, Azores (Cole et al. 2001). In wet phreatomagmatic eruptions, unlike at NPM, deformation associated with ballistic clasts can scale well beyond the size of the clast, and deformation associated with sediment loading is much more prevalent. Furthermore, the symmetrical, low-angle cross-strata at NPM commonly show

dominant accretion on the lee sides of the dunes; the infrequency of stoss-side grain accretions further supports the conclusion that little to no liquid water was present within the base surges (Crowe and Fisher 1973; Waters and Fisher 1971; Allen 1982; Sohn and Chough 1989; Chough and Sohn 1990; Dellino et al. 1990; Brand and White 2007).

The presence and abundance of vesicles within the fine ash component of the NPM deposits varies around the vent from 0% up to 20%. Vesicles in phreatomagmatic tuffs form by a gas phase trapped by the compaction of viscous, fine-grained wet ash (Fisher and Schmincke 1984). Potential sources of gas trapped in fine ash include juvenile volatiles released from hot pyroclasts; steam bubbles generated within a hot, dense wet ash matrix by deposition over hot pyroclastic material; air trapped by rapid accumulation of mud from a pyroclastic surge cloud (Lorenz 1974); or air trapped by the coalescence of accretionary lapilli (Rosi 1992). The most common interpretation for the occurrence of vesicles in phreatomagmatic tephras is trapped liquid water that was present in the eruption plume or density current during deposition (Lorenz 1974; Self et al. 1980; Rosi 1992). In this interpretation, vesicles are almost always found with other features indicative of liquid water, such as soft-sediment deformation and accretionary or armored lapilli. These features were not observed at NPM. Furthermore, it has been recently noted that the mechanisms by which vesicles form in ash is relatively unclear, and that they can form in fine-grained eolian soils in arid and semi-arid settings by non-volcanic mechanisms (McFadden et al. 1998). Therefore, the vesicles may have had less to do with liquid water at the time of deposition, and possibly more to do with post-emplacement formation, and thus not much significance is ascribed to them here.

Our observations at NPM indicate that little to no liquid water was present at the time of deposition. The external water involved in the eruption was largely converted to steam either during magma–water interaction, or shortly thereafter. We therefore interpret NPM to have been a dry phreatomagmatic eruption, likely with a melt–water mass ratio between 0.1 and 0.3 (Wohletz and McQueen 1984). Additionally, most of the juvenile material at NPM is present either as fine-lapilli scoria and pumice, or fine ash. The abundance of fine ash and its blocky, angular morphology in thin section indicates that the primary mechanism for fragmentation was magma–water interaction. However, the vesiculated juvenile clasts (with up to 60% vesicularity) implies that magmatic vesiculation occurred prior to or simultaneously with the phreatomagmatic fragmentation.

It is not feasible to determine if vesiculation of the melt also caused fragmentation, but this is a possibility. Similar features have been noted at Crater Hill, New Zealand, where a wide range of juvenile clast vesicularity (20–50%) was observed in the hydromagmatic deposits (Houghton et al. 1999). This observation was interpreted to indicate that vesiculation was already underway at the time of explosive magma–water interaction, but that vesiculation alone did not fragment the magma. Instead, explosions were thought to be driven by a combination of gas released from the rising magma and steam produced by the flashing of groundwater (Houghton et al. 1999; Houghton and Wilson 1989). Cole et al. (2001) also observed a wide range of clast vesicularity (up to 70% vesicles) within the juvenile pyroclasts in the hydromagmatic facies of the 1957–1958 Capelinhos eruption. They propose that while hydromagmatic fragmentation was dominant, vesiculation and fragmentation driven by magmatic volatiles operated simultaneously.

Vertical variation in the types of accidental lithics has been observed at other maar volcanoes, and is commonly attributed to downward coring of the diatreme as an eruption progresses (Lorenz 1982, 1986; Zimanowski 1986; Mastin 1991; Nemeth et al. 2001). Within each of the measured sections, distributed over three quadrants of NPM, accidental lithic species were dominated by individual grains of the Narbona Pass Member and by hypabyssal minette associated with subsurface dikes and sills. The cumulative proportion of entrained lithics originating from sedimentary units below the Narbona Pass Member was minor, and generally remained the same or decreased up-section. These trends in accidental lithic proportions suggest that the eruption did not result in excavation below the friable portion of the Narbona Pass Member, or no more than about 360 m below the surface at the time of eruption. By comparison, Ship Rock and surrounding minette diatremes on the Four Corners Platform, a few tens of kilometers to the east and northeast and similar to NPM in age and petrology, penetrated to depths of at least 1,000 m, as evidenced by their stratigraphic level of exhumation (Delaney 1987; Semken 2003).

The depth at which phreatomagmatic explosions occur in maar-diatreme volcanoes is controlled by the hydrostatic pressure and availability of external water (Lorenz 1986). Explosions are favored at pressures of 2 to 3 MPa (Fisher and Schmincke 1984; Lorenz 1986; Schmincke 2000; Zimanowski and Buettner 2003), corresponding to depths of a few tens to several hundred meters depending on geological conditions (Lorenz 1986; Lorenz and Kurszlaukis 2007; Lorenz and Haneke 2004). Magma may ascend unaffected through deep aquifers until it encounters this pressure threshold. The Lorenz model (Lorenz 1986; Lorenz and Kurszlaukis 2007) holds that a cone of depression forms in the water table surrounding the diatreme as the hydrovolcanic activity draws the aquifer down. This locally decreases hydrostatic pressure, allowing the zone of interaction to migrate downward and the explosive eruption to continue, as long as external water remains available. An example of this process is Tihany-style hydrovolcanism

(Nemeth et al. 2001), in which an eruption begins in a shallow aquifer, then excavates deeper to another aquifer as the initial source is depleted.

This hydrogeologic control may account for the comparatively shallow penetration of the diatreme eruption at NPM, which is structurally separated from the Four Corners Platform by the East Defiance monocline. Along this monocline in Laramide time, about 40 My before NVF activity, Mesozoic and older sedimentary units were steeply down-folded to the east (Cather 2003; Fig. 10a). The uppermost part of this section consists of interbedded sandstones and mudstones deposited by two major transgressions and subsequent regressions of the Late Cretaceous Western Interior Seaway (e.g., Eaton and Nations 1991). The basal transgressive mudstone in this sequence, the Mancos Shale, forms the land surface in the vicinity of Ship Rock, and as described above, directly underlies the Chuska Sandstone in the vicinity of NPM. The Mancos Shale is an aquiclude, but five Cretaceous sandstone aquifers, totaling about 300 m in thickness, intertongue with it or overlie it (Stone et al. 1983). All of these units dip shallowly to the east and crop out today between the East Defiance monocline and the edge of the San Juan structural basin about 50 km farther east. Erosional remnants of the second deepest of these aquifers, the Point Lookout Sandstone, sit in place on the north side of Ship Rock monolith about 150 m above the base, and hold up several surrounding mesas and buttes.

Paleogeomorphic studies by Cather et al. (2008) indicate that by about 35 Ma, the Defiance uplift and surrounding areas had been eroded to a nearly flat surface, upon which the Chuska erg aggraded from about 33.5 to 27 Ma. NVF eruptions commenced near the end of this interval (Semken 2003). As Fig. 10b shows, a thicker Cretaceous section, including the sandstone aquifers within and above the Mancos Shale aquiclude, was preserved to the east of the monocline. West of the monocline on the Defiance uplift, where NPM erupted, the uppermost Cretaceous units were eroded away by 35 Ma, and the Chuska Sandstone was deposited directly on the Mancos Shale aquiclude. Therefore, although Ship Rock and the other Four Corners Platform diatremes probably initiated in the Chuska Sandstone as did NPM, the additional aquifers underlying the Four Corners Platform could have enabled these diatremes to penetrate farther than NPM did.

This interpretation implies that local aquifer structure and stratigraphy control the depth to which a diatreme can penetrate. At NPM, the observed thick sequence of tuffs suggests that while magma–water interaction remained comparatively shallow, it was not short-lived. Rapid groundwater recharge in the Chuska Sandstone (weakly cemented and porous in the vicinity of NPM) would have allowed phreatomagmatic activity to continue without quickly depleting the aquifer or excavating more deeply into the subsurface.

The minimal post-eruptive erosion of NPM, compared to the deep exhumation of the Four Corners Platform diatremes (Fig. 10c), may be a consequence of subsequent regional silica cementation of the Chuska Sandstone which, while holding up the Chuska Mountains against incision of the Colorado Plateau in the Late Oligocene to Holocene (Cather et al. 2008), would also have better preserved the NVF volcanoes that erupted therein.

An alternative explanation is that the zone of magma–water interaction and fragmentation did core deeper into stronger country rocks but did not entrain them. We find this alternative less likely because the Chuska Sandstone in the vicinity of NPM is underlain by the equally or more friable Mancos Shale and Dakota Sandstone. If the diatreme had cored more deeply beneath NPM, these units should have been included in higher proportions throughout the pyroclastic section.

Valentine and Groves (1996) had a similar finding in the Lucero volcanic field, where the accidental clast component of three basaltic volcanoes comprised of hydrovolcanic, strombolian, and effusive products were studied in detail. They found that crustal xenoliths entrained below 500 m depth were equally represented in both the hydromagmatic and magmatic facies, but inclusions of the uppermost unit, the 500-m thick Chinle Formation, varied in proportion between these facies. Valentine and Groves (1996) suggested that the deeper country rocks were entrained by dike offshoots, or cracking of wall rock by thermal stresses and pore-pressure build-up, whereas the hydromagmatic activity entrained only the uppermost unit, the Chinle Formation. Similarly, we interpret xenoliths of deeper crustal and mantle rocks at NPM to have been entrained by the minette magma below the site of explosive activity.

Thus one of the more important findings at NPM is evidence for little downward excavation of the diatreme (<360 m) relative to other well-preserved, thick, hydromagmatically fragmented tuff sequences, many of which resulted from coring to depths of hundreds of meters to more than a kilometer (i.e., Lorenz 1986; Delaney 1987; Nemeth et al. 2001).

Clast composition, proportion, and dominant depositional mechanism varied azimuthally around the vent. Because the deposits are interpreted to be primarily the result of pyroclastic density currents, with only small portions derived from airfall, this asymmetry was not caused by changes in wind direction during emplacement. Instead, the asymmetry probably developed from multiple vents, from a single asymmetric vent, or from a migrating or widening vent encountering asymmetry in subsurface units. East–west migration of the focus of magma–water interaction could have caused the predominant accidental clast composition to

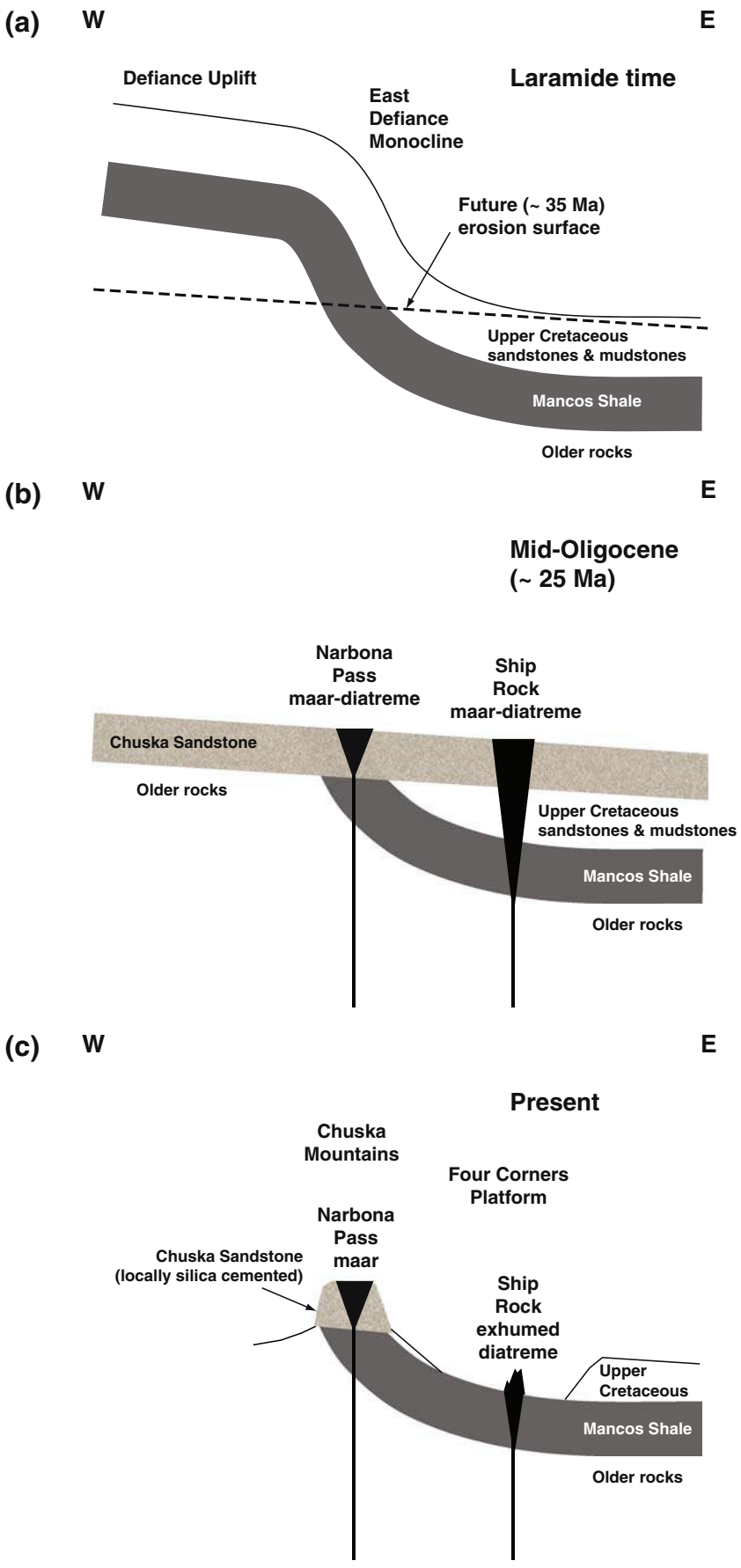

Fig. 10 **a** During the Laramide orogeny, Mesozoic and older strata were folded in the East Defiance Monocline in the vicinity of the future NPM. **b** By the middle Oligocene Epoch, the Defiance uplift had been eroded to a slightly eastward-dipping surface, upon which the Chuska Sandstone was deposited (Cather et al. 2008). Because of the removal of the west limb of the monocline, the Chuska Sandstone directly overlies the Mancos Shale aquiclude in the vicinity of the future NPM, whereas it overlies a thicker Upper Cretaceous section, including several aquifers, to the east. Therefore, Ship Rock and other NVF diatremes in its vicinity cored deeper than did the diatreme at Narbona Pass. **c** Deep erosion of the Colorado Plateau followed NVF activity. The Chuska Mountains and NPM have been held up by localized silica cementation of the Chuska Sandstone (Cather et al. 2008). In contrast, Ship Rock and its neighbors have been exhumed almost to their root zones

vary as observed, especially if minette dikes and sills in the feeder system have a preferred orientation (e.g., subparallel to the roughly north–south trend of the East Defiance monocline). This is most apparent in the East section where the base contains between 25–30% hypabyssal clasts, which quickly spike to 80% towards the lower-middle part of the section, and then drop to ~50% at the top of the section. This spike does not occur in any other sections around the edifice, and likely reflects the vent (or vents) encountering hypabyssal minette intrusions.

We further suggest that where the vent encountered these intrusions, less external water was available, and deposition occurred under comparatively drier conditions. Evidence of this was observed on the east and southeast sides of NPM, where hypabyssal minette lithics dominate, soft-sediment deformation features are essentially absent, and the deposits are interpreted to have been emplaced with little to no liquid water in the eruption column or flows. On the other hand, the west side deposits are dominated by lithics from the Chuska Sandstone, a porous, permeable aquifer, and, accordingly, exhibit wetter depositional features in the form of a higher proportion of ballistic clasts with bomb sags. An alternative explanation for the variation in wet features could be a change in the magma mass flux with respect to available external water. However, this interpretation does not account for the azimuthal variation in accidental lithics. Therefore, we prefer the former interpretation.

We also found that the slightly wetter western section is dominated by a combination of both dilute and concentrated density currents (PH3), whereas the comparatively drier east–northeast and southeastern sections are dominated by dilute density currents (the base surges of PH2; Figs. 7c, 8c and 9c). Can this observed variation in dominant depositional mechanism be related to source conditions, specifically to the subsurface lithology and available external water? Low vent velocities, syn-eruptive enlarging or widening of the vent, a high solid–gas ratio, and large grain sizes favor the formation of pyroclastic density currents (Wilson et al. 1978; Fisher and Schmincke 1984; Cas and Wright 1987), which may occur as concentrated or dilute flows. In general terms, the style, concentration, and

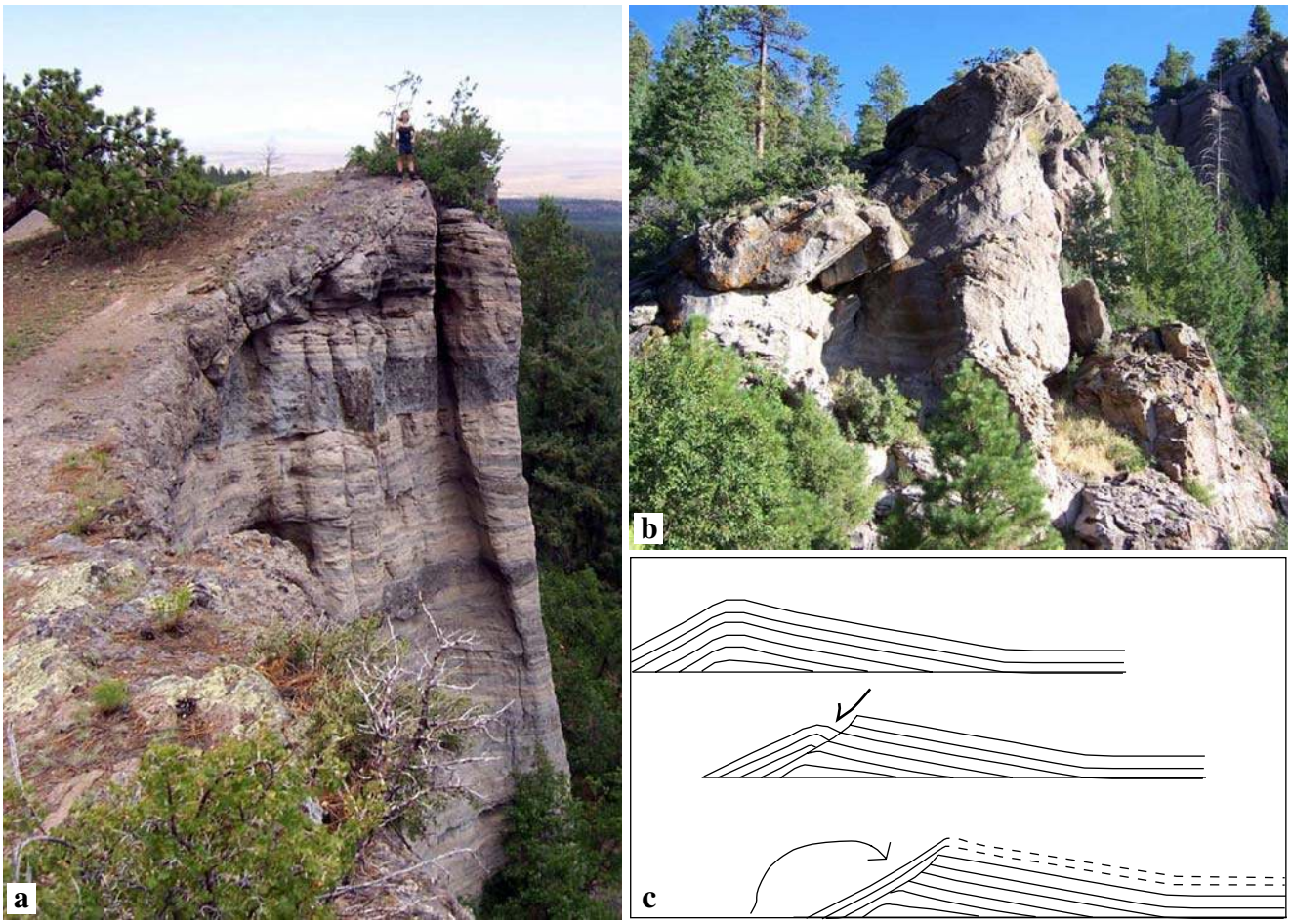

Fig. 11 The truncated tuff ring of NPM. **a** At the top of the southeast measured section (person approximately 1.5 m tall visible on the rim). **b** In the east rim of the crater near locality 3 in Fig. 1b (outcrop 25 m tall). **c** Schematic diagram illustrating the progression of the inner crater faulting and slumping towards vent during crater widening, and subsequent deposition of new material that truncates older strata

flow conditions of pyroclastic currents can be controlled by many additional factors, such as initial grain size distribution at the source and subsequent lateral transformation (e.g., Fisher 1966, 1979); changes in local flow conditions imposed by topographic variation; or preferred flow directions of an eruption (e.g., directed blasts). Here we speculate that at NPM, there may have been an additional control: the greater volume of water available from the Chuska Sandstone aquifer at the source of the western section deposits may have resulted in a higher proportion of concentrated pyroclastic currents to the west.

Another important observation at NPM is that the older deposits of the crater walls are truncated by younger deposits (Fig. 11), which is evidence for syn-eruptive crater widening. Widening of the crater could be interpreted as a consequence of downward penetration of the diatreme and concomitant widening of the crater diameter (Lorenz 1986), lateral migration of a single vent, widening of a single vent without concurrent downward coring, or the development of multiple vents over the course of the eruption. Based on entrained lithic proportions and lack of evidence for downward excavation of the crater, except that which may have occurred in the uppermost Narbona Pass Member, we interpret the syn-eruptive crater widening to represent either a vent that simply widened without deepening, or a vent that migrated laterally throughout the eruption.

Finally, this is the first study to document a significant magmatic volatile component (evidenced by the juvenile pumice and scoria) in NVF minette extrusives. Such volatiles may also have been present in other NVF minette eruptions, such as Ship Rock: a minette tuff-breccia diatreme intruded and flanked by minor minette plugs and dikes, suggesting an NPM-like history of pyroclastic eruption followed by extrusion of minette lavas (Delaney 1987). Was the fragmentation within these other eruptive centers driven solely by magma–water interaction, or did magmatic volatiles also play a role? Melt inclusion studies on NVF magmas, outside the scope of this work, should help answer this question and provide more information on the long-debated relationships between mantle hydration or metasomatism and Colorado Plateau magmatism (e.g., Smith et al. 2004; Humphreys et al. 2003).

Conclusions

A phreatomagmatic eruption occurred when minette magma interacted with groundwater within the permeable and friable Narbona Pass Member of the Chuska Sandstone, creating the Narbona Pass maar (NPM). The initial vent-clearing phase of the eruption produced concentrated pyroclastic density currents, followed by a period of pulsating dilute pyroclastic surges (base surges) and more concentrated currents, possibly accompanied by fallout. The final phase of the eruption produced three lava flows and three dome-like plugs. There is no evidence for a magmatic (i.e., Strombolian) phase or a long repose period between the phreatomagmatic and effusive phases. However, pillowed lava-flow features suggest that the crater contained water during lava flow emplacement.

Accretionary lapilli, soft sediment deformation, and stoss side accretion on dunes were absent or rare, suggesting that most of the external water was converted to steam either at the site of magma–water interaction or shortly after. The fine-grained, blocky and angular nature of the juvenile ash implies that the process of fragmentation was driven primarily by magma–water interaction, and that fragmentation was efficient. The presence of juvenile pumice and scoria, which generally composes between 20% and 45% of the clasts within the strata, suggests that the intruding magma was volatile rich and vesiculating at or near the time of eruption. This suggests that exsolution of magmatic volatiles may have been a secondary mechanism of fragmentation.

The vertical consistency of the deposits indicates that the influence of external water at the vent did not fluctuate significantly throughout the eruption. It also implies that the crater did not excavate beneath the uppermost country rock unit, the Narbona Pass Member of the Chuska Sandstone (<360 m below the paleosurface). Asymmetry within the deposit characteristics and dominant lithic composition azimuthally around the edifice likely resulted from a migrating or widening vent encountering asymmetry in subsurface units.

Acknowledgments We thank the Navajo Nation Minerals Department for permission to conduct field research at Narbona Pass. Anyone who wishes to conduct field investigations on the Navajo Nation must first apply for and receive a permit from the Navajo Nation Minerals Department in Window Rock, Navajo Nation, Arizona. We are especially grateful for the assistance of Cassandra Namingha in the field during summer 2005, and the steady support of Doris Bahee. Funding for this research was provided by a Geological Society of America Student Research Grant, an Arizona NASA Space Grant Consortium Student Fellowship, and the National Science Foundation, USA (EAR 0538125). The Division of Mathematics, Science, and Technology at Diné College, directed by Marnie Carroll, provided funding for C. Namingha's participation. This paper greatly benefited from thorough, thoughtful, and insightful reviews by Greg Valentine, Larry Mastin, and from the associate editor James White. Ahéhee' to all!

References

Allen JRL (1982) Sedimentary structures: their character and physical basis. Elsevier, Amsterdam, pp 395–431

Appledorn CR, Wright HE (1957) Volcanic structures in the Chuska Mountains, Navajo Reservation, Arizona–New Mexico. Geol Soc Amer Bull 68:445–468

Barwis JH, Hayes MO (1985) Antidunes on modern and ancient washover fans. J Sed Petrol 55:907–916

Best MG, Christiansen EH (2001) Igneous petrology. Blackwell Science, Malden, MA
Brand BD, White CM (2007) Origin and stratigraphy of phreatomagmatic deposits at the Pleistocene Sinker Butte Volcano, Western Snake River Plain, Idaho. J Volcanol Geotherm Res 160:319–339
Branney MJ, Kokelaar P (1992) A reappraisal of ignimbrite emplacement: progressive aggradation and changes from particulate to non-particulate flow during emplacement of high-grade ignimbrite. Bull Volcanol 54:504–520
Branney MJ, Kokelaar BP (2002) Pyroclastic density currents and the sedimentation of ignimbrites. Geol Soc Lond Mem 27:1–152
Bursik MI, Woods AW (1996) The dynamics and thermodynamics of large ash flows. Bull Volcanol 58:175–193
Büttner R, Dellino P, Zimanowski B (1999) Identifying magma–water interaction from the surface features of ash particles. Nature 401:688–690
Büttner R, Zimanowski B (1998) Physics of thermohydraulic explosions. Phys Rev E 57:5726–5729
Carlson RW, Nowell GM (2001) Olivine-poor sources for mantle-derived magmas: Os and Hf isotopic evidence from potassic magmas of the Colorado Plateau. Geochem Geophys Geosys 2 (6). doi:10.1029/2000GC000128
Cather SM (2003) The laramide defiance uplift. In: Lucas SG, Semken SC, Berglof WR, Ulmer-Scholle DS (eds) Geology of the Zuni Plateau: New Mexico. Geol Soc Guidebook 54:6–7
Cather SM, Peters L, Dunbar NW, McIntosh WC (2003) Genetic stratigraphy, provenance, and new age constraints for the Chuska Sandstone (Upper Eocene-Lower Oligocene), New Mexico-Arizona. In: Lucas SG, Semken SC, Berglof WR, Ulmer-Scholle DS (eds) Geology of the Zuni Plateau: New Mexico. Geol Soc Guidebook 54:397–412
Cather SM, Connell SD, Chamberlin RM, McIntosh WC, Jones GE, Potochnik AR, Lucas SG, Johnson PS (2008) The Chuska erg: paleogeomorphic and paleoclimatic implications of an Oligocene sand sea on the Colorado Plateau. Geol Soc Amer Bull 120: 13–33
Cas RAF, Wright JV (1987) Volcanic successions: modern and ancient. Alan & Unwin, London, pp 1–528
Chough SK, Sohn YK (1990) Depositional mechanics and sequences of base surges, Songaksan tuff ring, Cheju Island. Sedimentology 37:1115–1135
Cole PD (1991) Migration direction of sand-wave structures in pyroclastic-surge deposits; implications for depositional processes. Geology (Boulder) 19:1108–1111
Cole PD, Guest JE, Duncan AM, Pacheco J-M (2001) Capelinhos 1957–1958, Faial, Azores: deposits formed by an emergent surtseyan eruption. Bull Volcanol 63:204–220
Crowe BM, Fisher RV (1973) Sedimentary structures in base-surge deposits with special reference to cross-bedding, Ubehebe Craters, Death Valley, California. Geol Soc Amer Bull 84:663–682
Delaney PT (1987) Ship Rock, New Mexico: the vent of a violent volcanic eruption. In: Beus SS (ed) Geological society of America Centennial Field Guide, Rocky Mountain Section 2:411–415
Dellino P, Frazzetta G, La Volpe L (1990) Wet surge deposits at La Fossa di Vulcano; depositional and eruptive mechanisms. J Volcanol Geotherm Res 43:215–233
Doubik P, Hill BE (1999) Magmatic and hydromagmatic conduit development during the 1975 Tolbachik eruption, Kamchatka, with implications for hazards assessment at Yucca Mountain, NV. J Volcanol Geotherm Res 91:43–64
Drake TG (1990) Structural features in granular flows. J Geophys Res 95:8681–8696
Druitt TH (1992) Emplacement of the 18 May, 1980 lateral blast deposit east–northeast of Mount St. Helens, Washington. Bull Volcanol 54:554–572
Eaton JG, Nations JD (1991) Introduction: tectonic setting along the margin of the Cretaceous Western Interior Seaway, southwestern Utah and northern Arizona. Geol Soc Am Spec Pap 260:1–8
Ehrenberg SN (1978) Petrology of potassic volcanic rocks and ultramafic xenoliths from the Navajo volcanic field, New Mexico and Arizona. Ph.D. thesis, University of California at Los Angeles
Esperanca S, Holloway JR (1987) On the origin of some mica–lamprophyres; experimental evidence from a mafic minette. Contrib Mineral Petrol 95:207–216
Fisher RV (1966) Mechanism of deposition from pyroclastic flows. Am J Sci 264:350–363
Fisher RV (1979) Models for pyroclastic surges and pyroclastic flows. J Volcanol Geotherm Res 6:305–318
Fisher RV, Schmincke H-U (1984) Pyroclastic rocks. Springer, Berlin
Fisher R, Schmincke H (1994) Volcaniclastic sediment transport and deposition. Blackwell Scientific, Edinburgh
Fisher R, Waters AC (1970) Base surge bed forms in Maar volcanoes. Am Journ Sci 268:157–180
Freundt A, Bursik MI (2001) Pyroclastic flow and transport mechanisms. In: Freundt A, Rosi M (eds) From magma to tephra. Elsevier, Amsterdam, pp 25–51
Godchaux MM, Bonnichsen B, Jenks MD (1992) Types of phreatomagmatic volcanoes in the western Snake River Plain, Idaho, USA. J Volcanol Geotherm Res 52:1–25
Gonzales D, Burgess RT, Critchley MR, Turner BE (2006) New perspectives on the emplacement mechanisms involved in diatreme formation in the northeastern Navajo volcanic field, southwestern Colorado. Geol Soc Am Abstracts with Programs 38:4
Hanes DM, Bowen AJ (1985) A granular-fluid model for steady intense bed-load transport. J Geophys Res 90:9149–9158
Hein FJ (1982) Depositional mechanism of deep sea coarse clastic sediments, Cap Enrage Formation, Quebec. Can J Earth Sci 19:276–287
Heiken GH (1971) Tuff rings; examples from the Fort Rock-Christmas Lake valley basin, south-central Oregon. J Geophys Res 76:5615–5626
Houghton BF, Hackett WR (1984) Strombolian and phreatomagmatic deposits of Ohakune Craters, Ruapehu, New Zealand; a complex interaction between external water and rising basaltic magma. J Volcanol Geotherm Res 21:207–231
Houghton BF, Schmincke HU (1986) Mixed deposits of simultaneous strombolian and phreatomagmatic volcanism; Rothenberg Volcano, East Eifel volcanic field. J Volcanol Geotherm Res 30:117–130
Houghton BF, Wilson CJN (1989) A vesicularity index for pyroclastic deposits. Bull Volcanol 51:451–462
Houghton BF, Wilson CJN, Smith IEM (1999) Shallow-seated controls on styles of explosive basaltic volcanism; a case study from New Zealand. J Volcanol Geotherm Res 91:97–120
Humphreys E, Hessler E, Dueker K, Farmer GL, Erslev E, Atwater T (2003) How Laramide-age hydration of North American lithosphere by the Farallon Slab controlled subsequent activity in the Western United States. Inter Geol Rev 45:575–595
Jopling AV, Richardson EV (1966) Backset bedding developed in shooting flow in laboratory experiments. J Sed Petrol 36:821–825
Kneller BC, Branney MJ (1995) Sustained high-density turbidity currents and the deposition of thick massive sands. Sedimentology 42:607–616
Kokelaar P (1983) The mechanism of Surtseyan volcanism. J Geol Soc Lond 140:939–944
Kokelaar P (1986) Magma–water interactions in subaqueous and emergent basaltic volcanism. Bull Volcanol 48:275–289
Lin JT, Pao YH (1979) Wakes in stratified fluids. Ann Rev Fluid Mech 11:317–338
Lorenz V (1974) Vesiculated tuffs and associated features. Sedimentology 21:273–291
Lorenz V (1982) The 1977 explosive eruptions of the Ukinrek Maars, Alaska. Terra Cogn 2:205–206

Lorenz V (1986) On the growth of maars and diatremes and its relevance to the formation of tuff rings. Bull Volcanol 48:265–274

Lorenz V, Haneke J (2004) Relationship between diatremes, dykes, sills, laccoliths, intrusive-extrusive domes, lava flows, and tephra deposits with unconsolidated water-saturated sediments in the late Variscan intermontane Saar-Nahe Basin, SW Germany. Geol Soc Am Spec Pub 234:75–124

Lorenz V, Kurszlaukis S (2007) Root zone processes in the phreatomagmatic pipe emplacement model and consequences for the evolution of maar-diatreme volcanoes. J Volcanol Geotherm Res 159:4–32

Lowe D (1976) Subaqueous liquefied and fluidized sediment flows and their deposits. Sedimentology 23:285–308

Lowe D (1982) Sediment gravity flows II: depositional models with special reference to the deposits of high-density turbidity currents. J Sed Petrol 52:279–297

Lucas SG, Cather SM (2003) Stratigraphy of the Paleogene Chuska Sandstone, New Mexico-Arizona. In: Lucas SG, Semken SC, Berglof WR, Ulmer-Scholle DS (eds) Geology of the Zuni Plateau: New Mexico. Geol Soc Guidebook 54:397–412

Lucas SG, Semken SC, Heckert AB, Berglof WR, Hoffman G, Kues BS, Crumpler LS, Aubele JC (2003) First-day road log. In: Lucas SG, Semken SC, Berglof WR, Ulmer-Scholle DS (eds) Geology of the Zuni Plateau: New Mexico Geol Soc Guidebook 54:1–34

Mastin LG (1991) The roles of magma and groundwater in the phreatic eruptions at Inyo Craters, Long Valley Caldera, California. Bull Volcanol 53:579–596

Mastin LG (2007) The Generation of fine hydromagmatic ash by growth and disintegration of glassy rinds. J Geophys Res 112: 1–17

Mastin LG, Christiansen RL, Thornber C, Lowenstern J, Beeson M (2004) What makes hydromagmatic eruptions violent? Some insights from the Keanakako'i Ash, Kilauea Volcano, Hawai'i. J Volcanol Geotherm Res 137:15–31

McFadden LD, McDonald EV, Wells SG, Anderson JQ, Forman SL (1998) The vesicular layer and carbonate collars of desert soils and pavements: formation, age and relation to climate change. Geomorphology 24:101–145

Middleton GV (1965) Antidune cross-bedding in a large flume. J Sed Petrol 35:922–927

Nemeth K, White JDL (2003) Reconstructing eruption processes of a Miocene monogenetic volcanic field from vent remnants; Waipiata volcanic field, South Island, New Zealand. J Volcanol Geotherm Res 124:1–21

Nemeth K, Matrin U, Harangi Sz (2001) Miocene Phreatomagmatic volcanism at Tihany (Pannonian Basin, Hungary). J Volcanol Geotherm Res 111:111–135

Paola C, Wiele SM, Reinhart MA (1989) Upper-regime parallel lamination as the result of turbulent sediment transport and low-amplitude bed forms. Sedimentology 36:47–59

Postma G (1986) Classification for sediment gravity-flow deposits based on flow conditions during sedimentation. Geology (Boulder) 14:291–294

Roden MF (1981) Origin of coexisting minette and ultramafic breccia, Navajo volcanic field. Cont Min Petrol 77:195–206

Rosi M (1992) A model for the formation of vesiculated tuff by the coalescence of accretionary lapilli. Bull Volcanol 54:429–434

Schmidt K-H (1991) Tertiary palaeoclimatic history of the southeastern Colorado Plateau. Palaeogeogr Palaeoclimatol Palaeoecol 86:283–296

Schmincke H-U, Fisher RV, Waters A (1973) Antidune and chute and pool structures in the base surge deposits of the Laacher See area, Germany. Sedimentology 20:553–574

Self S, Kienle J, Huot JP (1980) Ukinrek Maars, Alaska, II: deposits and formation of the 1977 craters. J Volcanol Geotherm Res 7:39–65

Semken S (2003) Black rocks protruding up: the Navajo volcanic field. In: Lucas SG, Semken SC, Berglof WR, Ulmer-Scholle DS (eds) Geology of the Zuni Plateau: New Mexico. Geol Soc Guidebook 54:397–412

Shaanan U, Weinberger R, Navon O (2007) The relation between volatile-rich magma and phreatomagmatism: an example from Birket Ram, the Northern Golan. International Union of Geodesy and Geophysics Meeting XXIV, IAVCEI Scientific Program VS018:10

Sheridan MF, Wohletz KH (1983) Hydrovolcanism: Basic Considerations and Review. J Volcanol Geotherm Res 17:1–29

Smith D, Levy S (1976) Petrology of the Green Knobs diatreme and implications for the upper mantle below the Colorado Plateau. Earth Planet Sci Lett 29:107–125

Smith D, Connelly JN, Manser K, Moser DE, Housh TB, McDowell FW, Mack LE (2004) Evolution of Navajo eclogites and hydration of the mantle wedge below the Colorado Plateau, Southwestern United States. Geochem Geophys Geosyst 5: Q04005 DOI 10.1029/2003GC000675

Sohn YK (1997) On traction-carpet sedimentation. J Sed Res 67:502–509

Sohn YK, Chough SK (1989) Depositional processes of the Suwolbong tuff ring, Cheju Island (Korea). Sedimentology 36:837–855

Sparks RSJ (1976) Grain size variations in ignimbrites and implications for the transport of pyroclastic flows. Sedimentology 23:147–188

Sparks RSJ, Wilson L, Hulme G (1978) Theoretical modeling of the generation, movement, and emplacement of pyroclastic flows by column collapse. J Geophys Res 83:1727–1739

Stone WJ, Lyford FP, Frenzel PF, Mizell NH, Padgett ET (1983) Hydrogeology and water resources of San Juan Basin, New Mexico. Hydrologic Report, New Mexico Bureau of Mines and Mineral Resources 6:70

Trevena AS, Nash WP (1979) Chemistry and provenance of detrital plagioclase. Geology (Boulder) 7:475–478

U.S. Geological Survey map (1992) Narbona Pass, New Mexico. 1:24,000, 7.5 Minute Series. Washington DC

Valentine GA (1987) Stratified flow in pyroclastic surges. Bull Volcanol 49:616–630

Valentine GA, Giannetti B (1995) Single pyroclastic beds deposited by simultaneous fallout and surge processes; Roccamonfina Volcano, Italy. J Volcanol Geotherm Res 64:129–137

Valentine GA, Groves KR (1996) Entrainment of country rock during basaltic eruptions of the Lucero volcanic field, New Mexico. J Geol 104:71–90

Waters AC, Fisher RV (1971) Base surges and their deposits; Capelinhos and Taal volcanoes. J Geophys Res 76:5596–5614

White JDL (1996) Pre-emergent construction of a lacustrine basaltic volcano, Pahvant Butte, Utah (USA). Bull Volcanol 58:249–262

White JDL (2001) Eruption and reshaping of Pahvant Butte Volcano in Pleistocene Lake Bonneville. Spec Pub Int Assoc Sed 30:61–80

Wilson L, Sparks RSJ, Huang TC, Watkins ND (1978) The control of volcanic column heights by eruption energetics and dynamics. J Geophys Res 83:1829–1836

Wohletz KH, McQueen RG (1984) Experimental studies of hydromagmatic volcanism. Studies of geophysics. National Academy, Washington, DC, pp 158–169

Wohletz KH, Sheridan MF (1979) Model of pyroclastic surge. Geol Soc Am Spec Pap 180:177–194

Wright HE (1956) Origin of the Chuska sandstone, Arizona–New Mexico; a structural and petrographic study of a Tertiary eolian sediment. Geol Soc Amer Bull 67:413–434

Zimanowski B (1986) Fragmentations prozesse beim explosiven Vulkanismus in der Westeifel. Dr rer nat Thesis, Joh Gutenberg-Universität Mainz

Zimanowski B, Buettner R (2003) Phreatomagmatic explosions in subaqueous volcanism. Geophys Monograph 140:51–60

Zimanowski B, Fröhlich G, Lorenz V (1991) Quantitative experiments on phreatomagmatic explosions. J Volcanol Geotherm Res 48:341–358